



Calculation of predictions for non-identical particle correlations in heavy ions collisions at LHC energies from hydrodynamics-inspired models

MASTER OF SCIENCE THESIS

Author:
Mateusz Wojciech Gałażyn

Supervisor:
Prof. Adam Kisiel

Warsaw, 29th October 2014



Wyznaczenie przewidywań teoretycznych dla korelacji cząstek nieidentycznych w zderzeniach ciężkich jonów przy energiach LHC w modelach opartych na hydrodynamice

PRACA MAGISTERSKA

Autor:
Mateusz Wojciech Gałażyn

Promotor:
dr hab. inż. Adam Kisiel, prof. PW

Warszawa, 29 października 2014

Abstract

Streszczenie

Contents

4	1 Theory of heavy ion collisions	2
5	1.1 The Standard Model	2
6	1.2 Quantum Chromodynamics	3
7	1.2.1 Quarks and gluons	3
8	1.2.2 Quantum Chromodynamics potential	4
9	1.2.3 The quark-gluon plasma	6
10	1.3 Relativistic heavy ion collisions	7
11	1.3.1 Stages of heavy ion collision	7
12	1.3.2 QGP signatures	9
13	Elliptic flow	10
14	Transverse radial flow	12
15	Direct photons	13
16	Puzzle in di-lepton mass spectrum	15
17	Jet quenching	16
18	2 Therminator model	17
19	2.1 (3+1)-dimensional viscous hydrodynamics	17
20	2.2 Statistical hadronization	18
21	2.2.1 Cooper-Frye formalism	19
22	3 Particle interferometry	21
23	3.1 HBT interferometry	21
24	3.2 Theoretical approach	22
25	3.2.1 Conventions used	22
26	3.2.2 Two particle wave function	23
27	3.2.3 Source emission function	24
28	Relationship between one-dimensional and three-dimensional source sizes	25
29	3.2.4 Theoretical correlation function	26
30	3.2.5 Spherical harmonics decomposition of a correlation function	27
31	3.3 Experimental approach	28
32	3.4 Scaling of femtoscopic radii	29
33	3.4.1 Scaling in LCMS	30

35	3.4.2 Scaling in PRF	30
36	4 Results	32
37	4.1 Identical particles correlations	32
38	4.1.1 Spherical harmonics components	32
39	4.1.2 Centrality dependence of a correlation function	36
40	4.1.3 k_T dependence of a correlation function	36
41	4.2 Results of the fitting procedure	37
42	4.2.1 Femtoscopic radii scaling with the transverse mass	37
43	4.3 Discussion of results	42
44	5 Summary	43

⁴⁵ **Introduction**

⁴⁶ **Chapter 1**

⁴⁷ **Theory of heavy ion collisions**

⁴⁸ **1.1 The Standard Model**

⁴⁹ In the 1970s, a new theory of fundamental particles and their interaction
⁵⁰ emerged. A new concept, which concerns the electromagnetic, weak and strong
⁵¹ nuclear interactions between known particles. This theory is called *The Standard*
⁵² *Model*. There are seventeen named particles in the standard model, organized
⁵³ into the chart shown below (Fig. 1.1). Fundamental particles are divided into
two families: *fermions* and *bosons*.

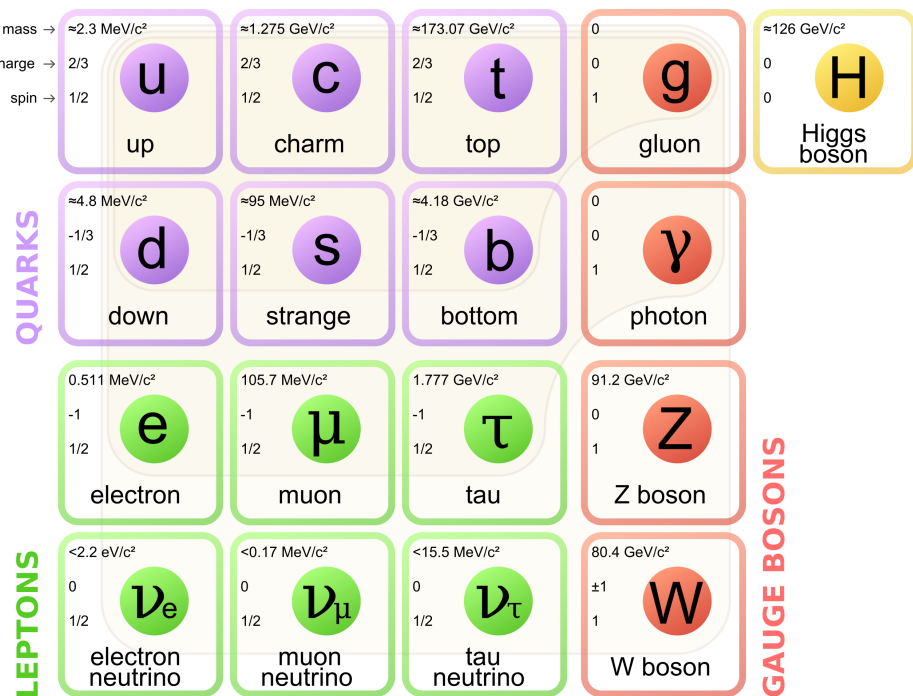


Figure 1.1: The Standard Model of elementary particles [1].

54 Fermions are the building blocks of matter. They are divided into two groups.
 55 Six of them, which must bind together are called *quarks*. Quarks are known to
 56 bind into doublets (*mesons*), triplets (*baryons*) and recently confirmed four-quark
 57 states.¹ Two of baryons, with the longest lifetimes, are forming a nucleus: a pro-
 58 ton and a neutron. A proton is build from two up quarks and one down, and
 59 neutron consists of two down quarks and one up. A proton is found to be a stable
 60 particle (at least it has a lifetime larger than 10^{35} years) and a free neutron has a
 61 mean lifetime about 8.8×10^2 s. Fermions, that can exist independently are called
 62 *leptons*. Neutrinos are a subgroup of leptons, which are only influenced by weak
 63 interaction. Fermions can be divided into three generations (three columns in
 64 the Figure 1.1). Generation I particles can combine into hadrons with the longest
 65 life spans. Generation II and III consists of unstable particles which form also
 66 unstable hadrons.

67 Bosons are force carriers. There are four fundamental forces: weak - respons-
 68 ible for radioactive decay, strong - coupling quarks into hadrons, electromagnetic
 69 - between charged particles and gravity - the weakest, which causes the attraction
 70 between particles with a mass. The Standard Model describes the first three. The
 71 weak force is mediated by W^\pm and Z^0 bosons, electromagnetic force is carried by
 72 photons γ and the carriers of a strong interaction are gluons g . The fifth boson is
 73 a Higgs boson which is responsible for giving other particles mass.

74 1.2 Quantum Chromodynamics

75 1.2.1 Quarks and gluons

76 Quarks interact with each other through the strong interaction. The mediator
 77 of this force is a *gluon* - a massless and chargeless particle. In the quantum chro-
 78 modynamics (QCD) - theory describing strong interaction - there are six types of
 79 "charges" (like electrical charges in the electrodynamics) called *colours*. The col-
 80 ours were introduced because some of the observed particles, like Δ^- , Δ^{++} and
 81 Ω^- appeared to consist of three quarks with the same flavour (ddd , uuu and sss
 82 respectively), which was in conflict with the Pauli principle. One quark can carry
 83 one of the three colours (usually called *red*, *green* and *blue*) and antiquark one of
 84 the three anti-colours respectively. Only colour-neutral (or white) particles could
 85 exist. Mesons are assumed to be a colour-anticolour pair, while baryons are *red-*
 86 *green-blue* triplets. Gluons also are colour-charged and there are 8 types of gluons.
 87 Therefore they can interact with themselves [3].

¹The LHCb experiment at CERN in Geneva confirmed recently existence of $Z(4430)$ - a particle consisting of four quarks [2].

88 **1.2.2 Quantum Chromodynamics potential**

89 As a result of that gluons are massless, one can expect, that the static potential
 90 in the QCD will have the similar form like one in the electrodynamics e.g. $\sim 1/r$
 91 (through an analogy to photons). In reality the QCD potential is assumed to have
 92 the form of [3]

$$V_s = -\frac{4}{3} \frac{\alpha_s}{r} + kr, \quad (1.1)$$

93 where the α_s is a coupling constant of the strong force and the kr part is related
 94 with the *confinement*. In comparison to the electromagnetic force, a value of the
 95 strong coupling constant is $\alpha_s \approx 1$ and the electromagnetic one is $\alpha = 1/137$.

96 The fact that quarks does not exist separately, but they are always bound,
 97 is called a confinement. As two quarks are pulled apart, the linear part kr in
 98 the Eq. 1.1 becomes dominant and the potential becomes proportional to the dis-
 99 tance. This situation resembles stretching of a string. At some point, when the
 100 string is so large it is energetically favourable to create a quark-antiquark pair. At
 101 this moment such pair (or pairs) is formed, the string breaks and the confinement
 102 is preserved (Fig. 1.2).

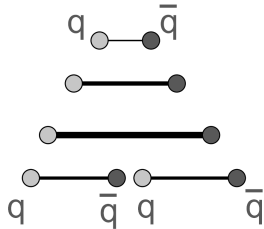


Figure 1.2: A string break and a creation of a pair quark-anti-quark [4].

102 On the other hand, for the small r , an interaction between the quarks and
 103 gluons is dominated by the Coulomb-like term $-\frac{4}{3} \frac{\alpha_s}{r}$. The coupling constant α_s
 104 depends on the four-momentum Q^2 transferred in the interaction. This depend-
 105 ence is presented in Fig. 1.3. The value α_s decreases with increasing momentum
 106 transfer and the interaction becomes weak for large Q^2 , i.e. $\alpha_s(Q) \rightarrow 0$. Be-
 107 cause of weakening of coupling constant, quarks at large energies (or small dis-
 108 tances) are starting to behave like free particles. This phenomenon is known as
 109 an *asymptotic freedom*. The QCD potential has also temperature dependence - the
 110 force strength “melts” with the temperature increase. Therefore the asymptotic
 111 freedom is expected to appear in either the case of high baryon densities (small
 112 distances between quarks) or very high temperatures. This temperature depend-
 113 ence is illustrated in the Fig. 1.4.

114 If the coupling constant α_s is small, one can use perturbative methods to cal-
 115 culate physical observables. Perturbative QCD (pQCD) successfully describes
 116 hard processes (with large Q^2), such as jet production in high energy proton-
 117 antiproton collisions. The applicability of pQCD is defined by the *scale parameter*

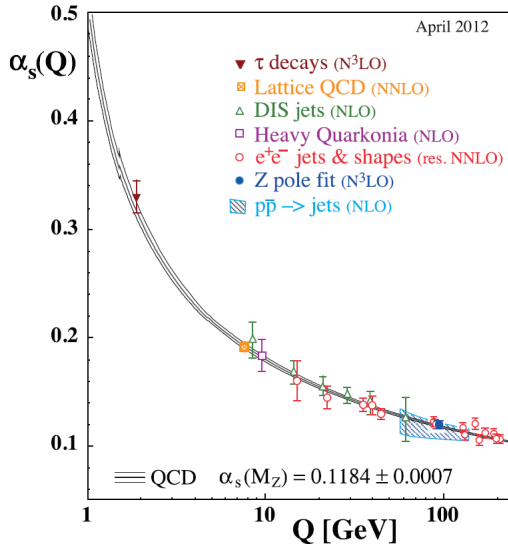


Figure 1.3: The coupling parameter α_s dependence on four-momentum transfer Q^2 [5].

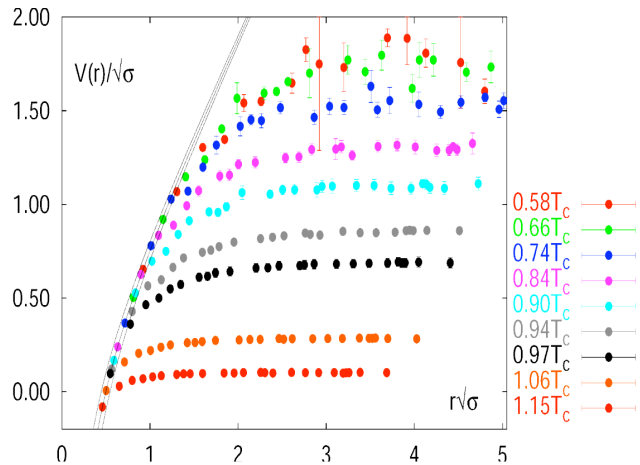


Figure 1.4: The QCD potential for a pair quark-antiquark as a function of distance for different temperatures. A value of a potential decreases with the temperature [4].

¹¹⁹ $\Lambda_{QCD} \approx 200$ MeV. If $Q \gg \Lambda_{QCD}$ then the process is in the perturbative domain
¹²⁰ and can be described by pQCD. A description of soft processes (when $Q < 1$ GeV)
¹²¹ is a problem in QCD - perturbative theory breaks down at this scale. Therefore,
¹²² to describe processes with low Q^2 , one has to use alternative methods like Lattice
¹²³ QCD. Lattice QCD (LQCD) is non-perturbative implementation of a field theory
¹²⁴ in which QCD quantities are calculated on a discrete space-time grid. LQCD al-

lows to obtain properties of matter in equilibrium, but there are some limitations. Lattice QCD requires fine lattice spacing to obtain precise results - therefore large computational resources are necessary. With the constant growth of computing power this problem will become less important. The second problem is that lattice simulations are possible only for baryon density $\mu_B = 0$. At $\mu_B \neq 0$, Lattice QCD breaks down because of the sign problem [6].

1.2.3 The quark-gluon plasma

The new state of matter in which quarks are no longer confined is known as a *quark-gluon plasma* (QGP). The predictions coming from the discrete space-time Lattice QCD calculations reveal a phase transition from the hadronic matter to the quark-gluon plasma at the high temperatures and baryon densities. The res-

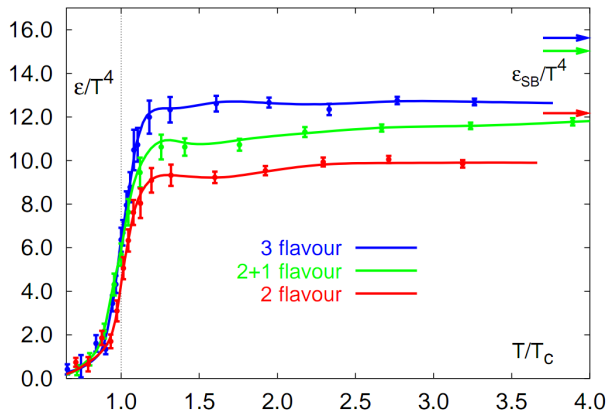


Figure 1.5: A number of degrees of freedom as a function of a temperature [7].

ults obtained from such calculations are shown on Fig. 1.5. The energy density ϵ which is divided by T^4 is a measure of number of degrees of freedom in the system. One can observe significant rise of this value, when the temperature increases past the critical value T_C . Such increase is signaling a phase transition - the formation of QGP [8]. The values of the energy densities plotted in Fig. 1.5 do not reach the Stefan-Boltzmann limit ϵ_{SB} (marked with arrows), which corresponds to an ideal gas. This can indicate some residual interactions in the system. According to the results from the RHIC², the new phase of matter behaves more like an ideal fluid, than like a gas [9].

One of the key questions, to which current heavy ion physics tries to find an answer is the value of a critical temperature T_C as a function of a baryon chemical potential μ_B (baryon density), where the phase transition occur. The results coming from the Lattice QCD are presented in the Fig. 1.6. The phase of matter in which quarks and gluons are deconfined is expected to exist at large

²Relativistic Heavy Ion Collider at Brookhaven National Laboratory in Upton, New York

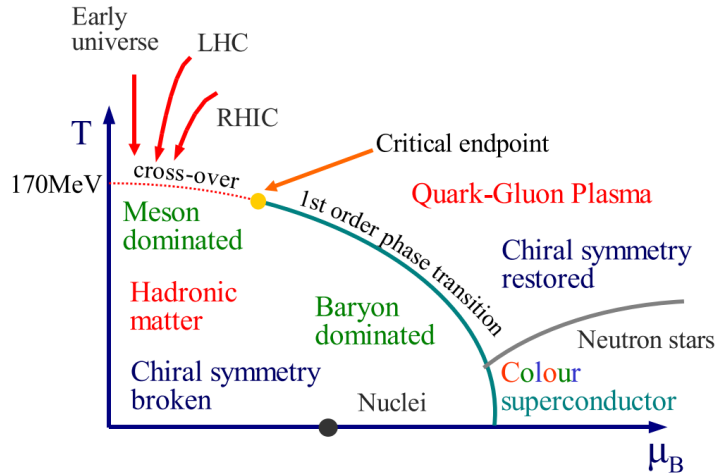


Figure 1.6: Phase diagram coming from the Lattice QCD calculations [8].

temperatures. In the region of small temperatures and high baryon densities, a different state is supposed to appear - a *colour superconductor*. The phase transition between hadronic matter and QGP is thought to be of 1st order at $\mu_B \gg 0$. However as $\mu_B \rightarrow 0$ quarks' masses become significant and a sharp transition transforms into a rapid but smooth cross-over. It is believed that in Pb-Pb collisions observed at the LHC³, the created matter has high enough temperature to be in the quark-gluon plasma phase, then cools down and converts into hadrons, undergoing a smooth transition [8].

1.3 Relativistic heavy ion collisions

1.3.1 Stages of heavy ion collision

To create the quark-gluon plasma one has to achieve high enough temperatures and baryon densities. Such conditions can be recreated in the heavy ion collisions at the high energies. The left side of the Figure 1.7 shows simplified picture of a central collision of two highly relativistic nuclei in the centre-of-mass reference frame. The colliding nuclei are presented as thin disks because of the Lorentz contraction. In the central region, where the energy density is the highest, a new state of matter - the quark-gluon plasma - is supposedly created. Afterwards, the plasma expands ad cools down, quarks combine into hadrons and their mutual interactions cease when the system reaches the *freeze-out* temperature. Subsequently, produced free hadrons move towards the detectors.

On the right side of the Figure 1.7 there is presented a space-time evolution of a collision process, plotted in the light-cone variables (z, t). The two highly

³Large Hadron Collider at CERN, Geneva

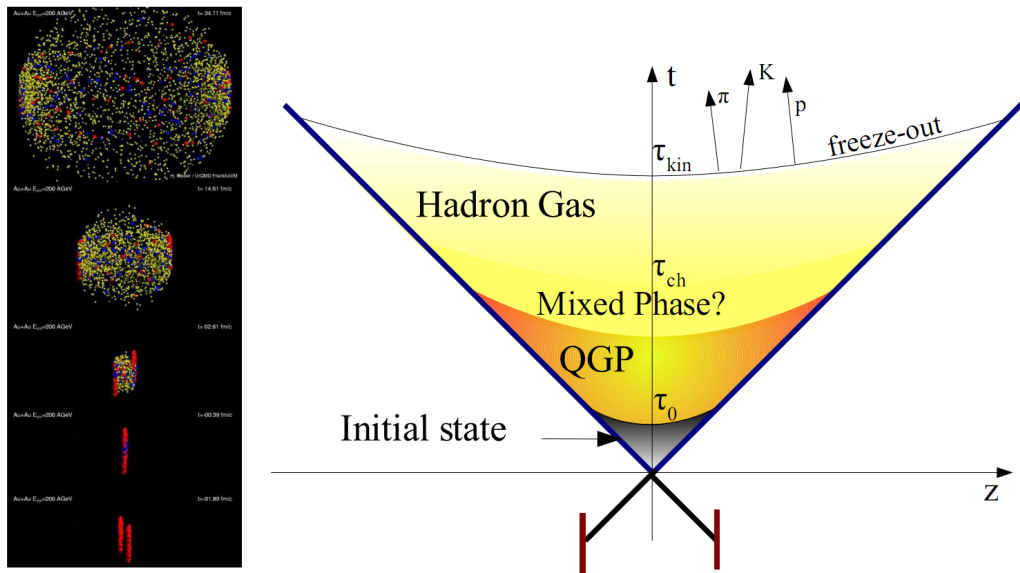


Figure 1.7: Left: stages of a heavy ion collision simulated in the UrQMD model. Right: schematic view of a heavy ion collision evolution [8].

172 relativistic nuclei are traveling basically along the light cone until they collide
 173 at the centre of diagram. Nuclear fragments emerge from the collision again
 174 along the (forward) light cone, while the matter between fragmentation zones
 175 populates the central region. This hot and dense matter is believed to be in the
 176 state of the quark-gluon plasma. There exist several frameworks to describe this
 177 transition to the QGP phase, for example: QCD string breaking, QCD parton cas-
 178 cades or colour glass condensate evolving into glasma and later into quark-gluon
 179 plasma [10].

180 **String breaking** – In the string picture, the nuclei pass through each other forming
 181 colour strings. This is analogous to the situation depicted in the Fig 1.2 - the
 182 colour string is created between quarks inside particular nucleons in nuclei. In
 183 the next step strings decay / fragment forming quarks and gluons or directly
 184 hadrons. This approach becomes invalid at very high energies, when the strings
 185 overlap and cannot be treated as independent objects.

186 **Parton cascade** – The parton⁴ cascade model is based on the pQCD. The col-
 187 liding nuclei are treated as clouds of quarks and which penetrate through each
 188 other. The key element of this method is the time evolution of the parton phase-
 189 space distributions, which is governed by a relativistic Boltzmann equation with
 190 a collision term that contains dominant perturbative QCD interations. The bot-
 191 tleneck of the parton cascade model is the low energies regime, where the Q^2 is
 192 too small to be described by the perturbative theory.

⁴A parton is a common name for a quark and a gluon.

193 **Colour glass condensate** – The colour glass condensate assumes, that the hadron can be viewed as a tightly packed system of interacting gluons. The saturation of gluons increases with energy, hence the total number of gluons may increase without the bound. Such a saturated and weakly coupled gluon system
 194 is called a colour glass condensate. The fast gluons in the condensate are Lorentz
 195 contracted and redistributed on the two very thin sheets representing two col-
 196 liding nuclei. The sheets are perpendicular to the beam axis. The fast gluons
 197 produce mutually orthogonal colour magnetic and electric fields, that only ex-
 198 ist on the sheets. Immediately after the collision, i.e. just after the passage of
 199 the two gluonic sheets after each other, the longitudinal electric and magnetic
 200 fields are produced forming the *glasma*. The glasma fields decay through the
 201 classical rearrangement of the fields into radiation of gluons. Also decays due to
 202 the quantum pair creations are possible. In this way, the quark-gluon plasma is
 203 produced.
 204

205 Interactions within the created quark-gluon plasma bring the system into the
 206 local statistical equilibrium, hence its further evolution can be described by the
 207 relativistic hydrodynamics. The hydrodynamic expansion causes that the sys-
 208 tem becomes more and more dilute. The phase transition from the quark-gluon
 209 plasma to the hadronic gas occurs. Further expansion causes a transition from the
 210 strongly interaction hadronic gas to weakly interacting system of hadrons which
 211 move freely to the detectors. Such decoupling of hadrons is called the *freeze-out*.
 212 The freeze-out can be divided into two phases: the chemical freeze-out and the
 213 thermal one. The *chemical freeze-out* occurs when the inelastic collisions between
 214 constituents of the hadron gas stop. As the system evolves from the chemical
 215 freeze-out to the thermal freeze-out the dominant processes are elastic collisions
 216 (such as, for example $\pi + \pi \rightarrow \rho \rightarrow \pi + \pi$) and strong decays of heavier reso-
 217 nances which populate the yield of stable hadrons. The *thermal freeze-out* is the
 218 stage of the evolution of matter, when the strongly coupled system transforms
 219 to a weakly coupled one (consisting of essentially free particles). In other words
 220 this is the moment, where the hadrons practically stop to interact. Obviously, the
 221 temperatures corresponding to the two freeze-outs satisfy the condition
 222

$$T_{chem} > T_{therm}, \quad (1.2)$$

223 where T_{chem} (inferred from the ratios of hadron multiplicities) is the temperature
 224 of the chemical freeze-out, and T_{therm} (obtained from the investigation of the
 225 transverse-momentum spectra) is the temperature of the thermal freeze-out [10].
 226

227 1.3.2 QGP signatures

228 The quark-gluon plasma is a very short living and unstable state of matter.
 229 One cannot investigate the properties of a plasma and confirm its existence di-
 230 rectly. Hence, the several experimental effects were proposed as QGP signatures,
 231 some of them have been already observed in heavy ion experiments [8]. As mat-
 232 ter created in the heavy ions collisions is supposed to behave like a fluid, one

should expect appearance of collective behaviour at small transverse momenta - so called *elliptic flow* and *radial flow*. The next signal is the temperature range obtained from the measurements of *direct photons*, which gives us information, that the system created in heavy ion collisions is far above the critical temperature obtained from the LQCD calculations. The *puzzle in the di-lepton spectrum* can be explained by the modification of spectral shape of vector mesons (mostly ρ meson) in the presence of a dense medium. This presence of a medium can also shed light on the *jet quenching* phenomenon - the suppression occurrence in the high p_T domain.

Elliptic flow

In a non-central heavy ion collisions, created region of matter has an almond shape with its shorter axis in the *reaction plane* (Fig. 1.8). The pressure gradient is much larger in-plane rather than out-of-plane. This causes larger acceleration and transverse velocities in-plane rather than out-of-plane. Such differences can

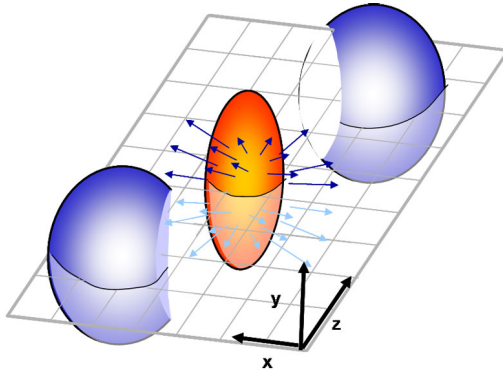


Figure 1.8: Overlapping region which is created in heavy ion collisions has an almond shape. Visible x-z plane is a *reaction plane*. The x-y plane is a *transverse plane*. The z is a direction of the beam [11].

be investigated by studying the distribution of particles with respect to the reaction plane orientation [12]:

$$E \frac{d^3 N}{dp^3} = \frac{1}{2\pi} \frac{d^2 N}{p_T dp_T dy} (1 + 2v_1 \cos(\phi) + 2v_2 \cos(2\phi) + \dots), \quad (1.3)$$

where ϕ is the angle between particle transverse momentum p_T (a momentum projection on a transverse plane) and the reaction plane, N is a number of particles and E is an energy of a particle. The y variable is a *rapidity* defined as:

$$y = \frac{1}{2} \ln \left(\frac{E + p_L}{E - p_L} \right), \quad (1.4)$$

252 where p_L is a longitudinal component of a momentum (parallel to the beam direction).
 253 The v_n coefficients indicate the shape of a system. For the most central collisions
 254 ($b = 0$ - see Fig. 1.9) all coefficients vanish $\bigwedge_{n \in N_+} v_n = 0$ (the overlapping region has the spherical shape). The Fourier series elements in the parentheses

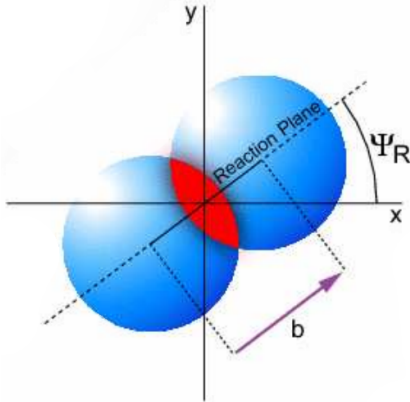


Figure 1.9: Cross-section of a heavy ion collision in a transverse plane. Ψ_R is an angle between transverse plane and the reaction plane. The b parameter is an *impact parameter* - a distance between centers of nuclei during a collision. An impact parameter is related with the centrality of a collision and a volume of the quark-gluon plasma [12].

255 in Eq. 1.3 represent different kinds of a flow. The first value: "1" represents the
 256 *radial flow* - an isotropic flow in every direction. Next coefficient v_1 is responsible
 257 for *direct flow*. The v_2 coefficient is a measure of elliptic anisotropy (*elliptic flow*).
 258 The v_2 has to build up in the early stage of a collision - later the system becomes
 259 too dilute: space asymmetry and the pressure gradient vanish. Therefore the
 260 observation of elliptic flow means that the created matter was in fact a strongly
 261 interacting matter.

262 The v_2 coefficient was measured already at CERN SPS, LHC and RHIC. For
 263 the first time hydrodynamics successfully described the collision dynamics as the
 264 measured v_2 reached hydrodynamic limit (Fig. 1.10). As expected, there is a mass
 265 ordering of v_2 as a function of p_T (lower plot in the Fig. 1.10) with pions having
 266 the largest and protons the smallest anisotropy. In the upper plots in the Fig. 1.10
 267 there is a v_2 as a function of transverse kinetic energy. The left plot shows the
 268 two universal trend lines for baryons and mesons. After the scaling of v_2 and the
 269 kinetic energy by the number of valence quarks, all of the hadrons follow the
 270 same universal curve. Those plots show that strong collectivity is observed in
 271 heavy ion collisions.

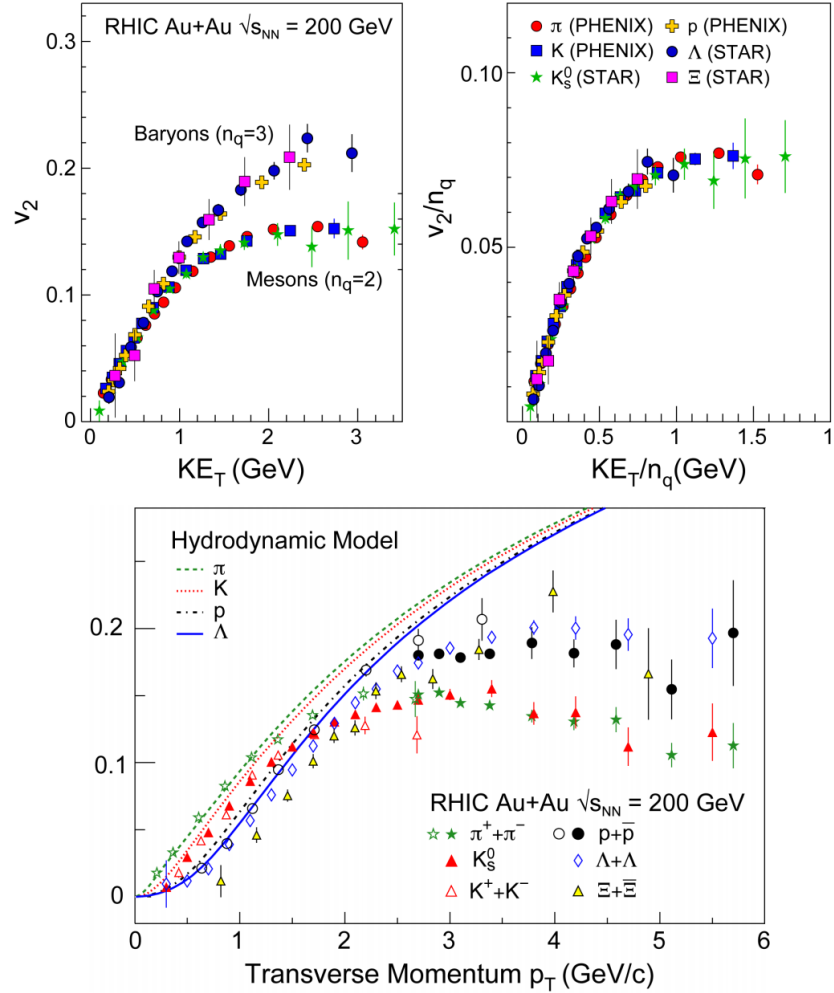


Figure 1.10: *Lower:* The elliptic flow v_2 follows the hydrodynamical predictions for an ideal fluid perfectly. Note that > 99% of all final hadrons have $p_T < 1.5$ GeV/c. *Upper left:* The v_2 plotted versus transverse kinetic energy $KE_T = m_T - m_0 = \sqrt{p_T^2 + m_0^2} - m_0$. The v_2 follows different universal curves for mesons and baryons. *Upper right:* When scaled by the number of valence quarks, the v_2 follows the same universal curve for all hadrons and for all values of scaled transverse kinetic energy [13].

273 Transverse radial flow

274 Elliptic flow described previously is caused by the pressure gradients which
 275 must also produce a more simple collective behaviour of matter - a movement
 276 inside-out, called radial flow. Particles are pushed to higher momenta and they
 277 move away from the center of the collision. A source not showing collective

278 behaviour, like pp collisions, produces particle spectra that can be fitted by a
279 power-law [8]:

$$\frac{1}{2\pi p_T} \frac{d^2N}{dp_T d\eta} = C \left(1 + \frac{p_T}{p_0} \right)^{-\gamma}. \quad (1.5)$$

280 The η variable is a *pseudorapidity* defined as follows:

$$\eta = \frac{1}{2} \ln \left(\frac{p + p_L}{p - p_L} \right) = -\ln \left(\frac{\theta}{2} \right), \quad (1.6)$$

where θ is an emission angle $\cos \theta = p_L/p$.

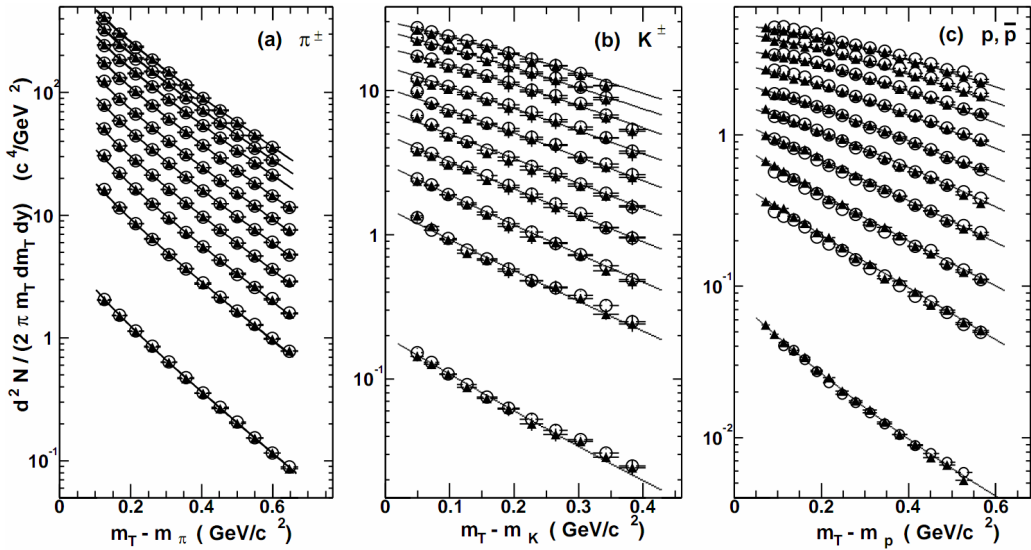


Figure 1.11: Invariant yield of particles versus transverse mass $m_T = \sqrt{p_T^2 + m_0^2}$ for π^\pm , K^\pm , p and \bar{p} at mid-rapidity for p+p collisions (bottom) and Au+Au events from 70-80% (second bottom) to 0-5% (top) centrality [14].

281
282 The hydrodynamical expansion of a system gives the same flow velocity kick
283 for different kind of particles - ones with bigger masses will gain larger p_T boost.
284 This causes increase of the yield of particles with larger transverse momenta. In
285 the invariant yield plots one can observe the decrease of the slope parameter,
286 especially for the heavier hadrons. This is presented in the Fig. 1.11. The most
287 affected spectra are ones of kaons (b) and protons (c). One can notice decrease
288 of the slope parameter for heavy ion collisions (plots from second bottom to top)
289 comparing to the proton-proton collisions (bottom ones), where no boost from
290 radial flow should occur [8].

291 Direct photons

292 The direct photons are photons, which are not coming from the final state
293 hadrons decays. Their sources can be various interaction from charged particles

created in the collision, either at the partonic or at the hadronic level. Direct photons are considered to be an excellent probe of the early stage of the collision. This is because their mean free path is very large to the created system in the collision. Thus photons created at the early stage leave the system without suffering any interaction and retain information about this stage, in particular about its temperature.

One can distinguish two kinds of direct photons: *thermal* and *prompt*. Thermal photons can be emitted from the strong processes in the quark-gluon plasma involving quarks and gluons or hot hadronic matter (e.g. processes: $\pi\pi \rightarrow \rho\gamma$, $\pi\rho \rightarrow \pi\gamma$). Thermal photons can be observed in the low p_T region. Prompt photons are believed to come from “hard” collisions of initial state partons belonging to the colliding nuclei. The prompt photons can be described using the pQCD. They will dominate the high p_T region. The analysis of transverse momentum of spectra of direct photons revealed, that the temperature of the source of thermal photons produced in heavy ion collisions at RHIC is in the range 300–600 MeV (Fig. 1.12). Hence the direct photons had to come from a system whose temperature is far above from the critical temperature for QGP creation.

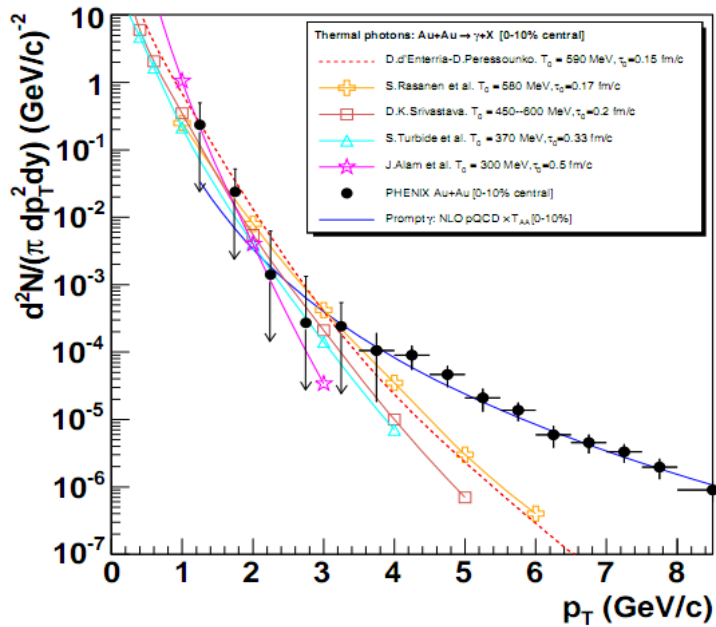


Figure 1.12: Thermal photons spectra for the central Au+Au collisions at $\sqrt{s_{NN}} = 200$ GeV computed within different hydrodynamical models compared with the pQCD calculations (solid line) and experimental data from PHENIX (black dots) [15].

311 **Puzzle in di-lepton mass spectrum**

312 The invariant mass spectra (Fig. 1.13) of lepton pairs reveal many peaks cor-
 313 responding to direct decays of various mesons into a lepton pair. The continu-
 314 ous background in this plot is caused by the decays of hadrons into more than
 315 two leptons (including so-called *Dalitz decays* into a lepton pair and a photon). Particular hadron decay channels, which contribute to this spectrum are shown

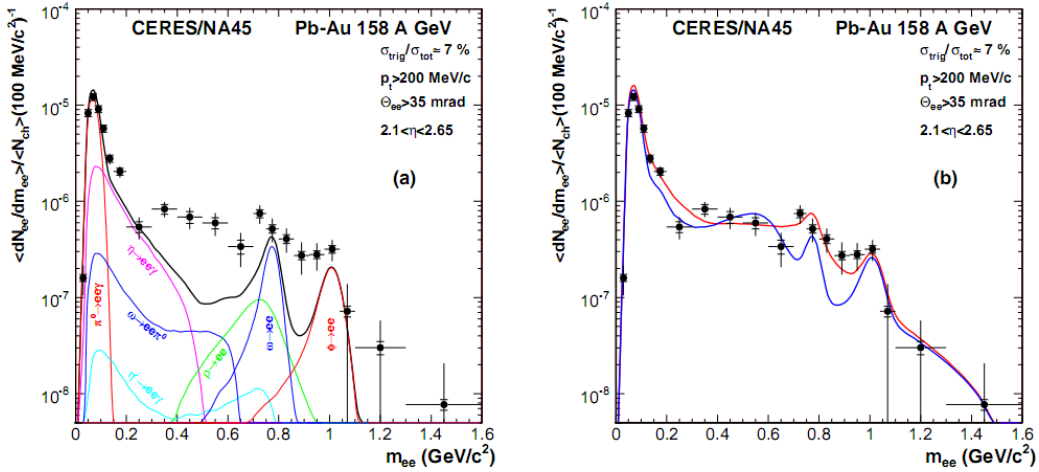


Figure 1.13: Left: Invariant mass spectrum of $e^+ - e^-$ pairs in $\text{Pb} + \text{Au}$ collisions at 158A GeV compared to the sum coming from the hadron decays predictions. Right: The expectations coming from model calculations assuming a dropping of the ρ mass (blue) or a spread of the ρ width in the medium [16].

316 in the Fig. 1.13 with the coloured lines and their sum with the black one. The
 317 sum (called *the hadronic cocktail*) of various components describes experimental
 318 spectra coming from the simple collisions (like $p + p$ or $p + A$) quite well with the
 319 statistical and systematical uncertainties [9]. This situation is different consider-
 320 ing more complicated systems i.e. $A + A$. Spectra coming from $\text{Pb} + \text{Au}$ collisions
 321 are presented on the plots in the Fig. 1.13. The “hadronic cocktail” does not de-
 322 scribe the data, in the mass range between the π and the ρ mesons a significant
 323 excess of electron pairs over the calculated sum is observed. Theoretical expla-
 324 nation of this phenomenon assumes modification of the spectral shape of vector
 325 mesons in a dense medium. Two different interpretations of this increase were
 326 proposed: a decrease of meson mass with the medium density and increase of the
 327 meson width in the dense medium. In principle, one could think of simultaneous
 328 occurrence of both effects: mass shift and resonance broadening. Experimental
 329 results coming from the CERES disfavour the mass shift hypothesis indicating
 330 only broadening of resonance peaks (Fig. 1.13b) [9].

332 **Jet quenching**

333 A jet is defined as a group of particles with close vector momenta and high en-
 334 ergies. It has its beginning when the two partons are going in opposite directions
 335 and have energy big enough to produce new quark-antiquark pair and then ra-
 336 diate gluons. This process can be repeated many times and it results in two back-
 337 to-back jets of hadrons. It has been found that jets in the opposite hemisphere
 338 (*away-side jets*) show a very different pattern in d+Au and Au+Au collisions. This
 339 is shown in the azimuthal correlations in the Fig. 1.14. In d+Au collisions, like in
 340 p+p, a pronounced away-side jet appears around $\Delta\phi = \pi$, exactly opposite to the
 341 trigger jet, what is typical for di-jet events. In central Au+Au collisions the away-
 jet is suppressed. When the jet has its beginning near the surface of the quark-

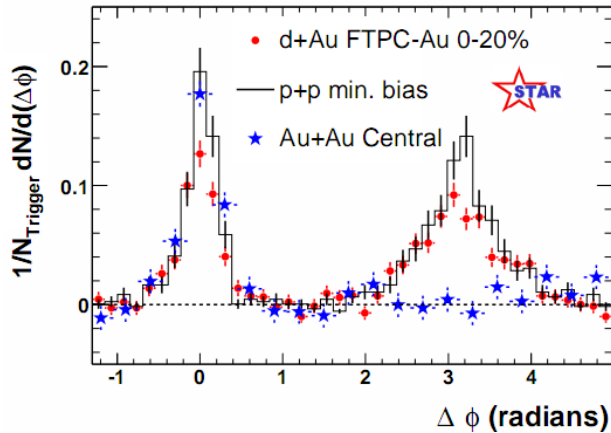


Figure 1.14: Azimuthal angle difference $\Delta\phi$ distributions for different colliding systems at $\sqrt{s_{NN}} = 200$ GeV. Transverse momentum cut: $p_T > 2$ GeV. For the Au+Au collisions the away-side jet is missing [17].

342 gluon plasma, one of the jets (*near-side jet*) leaves the system almost without any
 343 interactions. This jet is visible on the correlation plot as a high peak at $\Delta\phi = 0$.
 344 However, the jet moving towards the opposite direction has to penetrate a dense
 345 medium. The interaction with the plasma causes energy dissipation of particles
 346 and is visible on an azimuthal correlation plot as disappearance of the away-side
 347 jet [9].

349 **Chapter 2**

350 **Therminator model**

351 THERMINATOR [18] is a Monte Carlo event generator designed to investigate
352 the particle production in the relativistic heavy ion collisions. The functionality
353 of the code includes a generation of the stable particles and unstable resonances
354 at the chosen hypersurface model. It performs the statistical hadronization which
355 is followed by space-time evolution of particles and the decay of resonances. The
356 key element of this method is an inclusion of a complete list of hadronic reso-
357 nances, which contribute very significantly to the observables. The second version
358 of THERMINATOR [19] comes with a possibility to incorporate any shape of freeze-
359 out hypersurface and the expansion velocity field, especially those generated ex-
360 ternally with various hydrodynamic codes.

361 **2.1 (3+1)-dimensional viscous hydrodynamics**

362 Most of the relativistic viscous hydrodynamic calculations are done in
363 (2+1)-dimensions. Such simplification assumes boost-invariance of a matter
364 created in a collision. Experimental data reveals that no boost-invariant region is
365 formed in the collisions [20]. Hence, for the better description of created system
366 a (3+1)-dimensional model is required.

367 In the four dimensional relativistic dynamics one can describe a system
368 using a space-time four-vector $x^\nu = (ct, x, y, z)$, a velocity four-vector
369 $u^\nu = \gamma(c, v_x, v_y, v_z)$ and a energy-momentum tensor $T^{\mu\nu}$. The particular
370 components of $T^{\mu\nu}$ have a following meaning:

- 371 • T^{00} - an energy density,
- 372 • $cT^{0\alpha}$ - an energy flux across a surface x^α ,
- 373 • $T^{\alpha 0}$ - an α -momentum flux across a surface x^α multiplied by c ,
- 374 • $T^{\alpha\beta}$ - components of momentum flux density tensor,

375 where $\gamma = (1 - v^2/c^2)^{-1/2}$ is Lorentz factor and $\alpha, \beta \in \{1, 2, 3\}$. Using u^ν one can
 376 express $T^{\mu\nu}$ as follows [21]:

$$T_0^{\mu\nu} = (e + p)u^\mu u^\nu - pg^{\mu\nu} \quad (2.1)$$

377 where e is an energy density, p is a pressure and $g^{\mu\nu}$ is an inverse metric tensor:

$$g^{\mu\nu} = \begin{bmatrix} 1 & 0 & 0 & 0 \\ 0 & -1 & 0 & 0 \\ 0 & 0 & -1 & 0 \\ 0 & 0 & 0 & -1 \end{bmatrix}. \quad (2.2)$$

378 The presented version of energy-momentum tensor (Eq. 2.1) can be used to de-
 379 scribe dynamics of a perfect fluid. To take into account influence of viscosity,
 380 one has to apply the following corrections coming from shear $\pi^{\mu\nu}$ and bulk Π
 381 viscosities [22]:

$$T^{\mu\nu} = T_0^{\mu\nu} + \pi^{\mu\nu} + \Pi(g^{\mu\nu} - u^\mu u^\nu). \quad (2.3)$$

382 The stress tensor $\pi^{\mu\nu}$ and the bulk viscosity Π are solutions of dynamical equa-
 383 tions in the second order viscous hydrodynamic framework [21]. The compari-
 384 son of hydrodynamics calculations with the experimental results reveal, that the
 385 shear viscosity divided by entropy η/s has to be small and close to the AdS/CFT
 386 estimate $\eta/s = 0.08$ [22, 23]. The bulk viscosity over entropy value used in calcu-
 387 lations is $\zeta/s = 0.04$ [22].

388 When using $T^{\mu\nu}$ to describe system evolving close to local thermodynamic
 389 equilibrium, relativistic hydrodynamic equations in a form of:

$$\partial_\mu T^{\mu\nu} = 0 \quad (2.4)$$

390 can be used to describe the dynamics of the local energy density, pressure and
 391 flow velocity.

392 Hydrodynamic calculations are starting from the Glauber¹ model initial con-
 393 ditions. The collective expansion of a fluid ends at the freeze-out hypersurface.
 394 That surface is usually defined as a constant temperature surface, or equivalently
 395 as a cut-off in local energy density. The freeze-out is assumed to occur at the
 396 temperature $T = 140$ MeV.

397 2.2 Statistical hadronization

398 Statistical description of heavy ion collision has been successfully used
 399 to describe quantitatively *soft* physics, i.e. the regime with the transverse
 400 momentum not exceeding 2 GeV. The basic assumption of the statistical
 401 approach of evolution of the quark-gluon plasma is that at some point of the

¹The Glauber Model is used to calculate “geometrical” parameters of a collision like an impact parameter, number of participating nucleons or number of binary collisions.

space-time evolution of the fireball, the thermal equilibrium is reached. When the system is in the thermal equilibrium the local phase-space densities of particles follow the Fermi-Dirac or Bose-Einstein statistical distributions. At the end of the plasma expansion, the freeze-out occurs. The freeze-out model incorporated in the THERMINATOR model assumes, that chemical and thermal freeze-out occur at the same time.

2.2.1 Cooper-Frye formalism

The result of the hydrodynamic calculations is the freeze-out hypersurface Σ^μ . A three-dimensional element of the surface is defined as [19]

$$d\Sigma_\mu = \epsilon_{\mu\alpha\beta\gamma} \frac{\partial x^\alpha}{\partial \alpha} \frac{\partial x^\beta}{\partial \beta} \frac{\partial x^\gamma}{\partial \gamma} d\alpha d\beta d\gamma, \quad (2.5)$$

where $\epsilon_{\mu\alpha\beta\gamma}$ is the Levi-Civita tensor and the variables $\alpha, \beta, \gamma \in \{1, 2, 3\}$ are used to parametrize the three-dimensional freeze-out hypersurface in the Minkowski four-dimensional space. The Levi-Civita tensor is equal to 1 when the indices form an even permutation (eg. ϵ_{0123}), to -1 when the permutation is odd (e.g. ϵ_{2134}) and has a value of 0 if any index is repeated. Therefore [19],

$$d\Sigma_0 = \begin{vmatrix} \frac{\partial x}{\partial \alpha} & \frac{\partial x}{\partial \beta} & \frac{\partial x}{\partial \gamma} \\ \frac{\partial y}{\partial \alpha} & \frac{\partial y}{\partial \beta} & \frac{\partial y}{\partial \gamma} \\ \frac{\partial z}{\partial \alpha} & \frac{\partial z}{\partial \beta} & \frac{\partial z}{\partial \gamma} \end{vmatrix} d\alpha d\beta d\gamma \quad (2.6)$$

and the remaining components are obtained by cyclic permutations of t, x, y and z .

One can obtain the number of hadrons produced on the hypersurface Σ^μ from the Cooper-Frye formalism. The following integral yields the total number of created particles [19]:

$$N = (2s + 1) \int \frac{d^3 p}{(2\pi)^3 E_p} \int d\Sigma_\mu p^\mu f(p_\mu u^\mu), \quad (2.7)$$

where $f(p_\mu u^\mu)$ is the phase-space distribution of particles (for stable ones and resonances). One can simply derive from Eq. 2.7, the dependence of the momentum density [24]:

$$E \frac{d^3 N}{dp^3} = \int d\Sigma_\mu f(p_\mu u^\mu) p^\mu. \quad (2.8)$$

The momentum distribution f contains non-equilibrium corrections:

$$f = f_0 + \delta f_{shear} + \delta f_{bulk}, \quad (2.9)$$

where

$$f_0(p_\mu u^\mu) = \left\{ \exp \left[\frac{p_\mu u^\mu - (B\mu_B + I_3\mu_{I_3} + S\mu_S + C\mu_C)}{T} \right] \pm 1 \right\}^{-1} \quad (2.10)$$

427 In case of fermions, in the Eq. 2.10 there is a plus sign and for bosons, minus
 428 sign respectively. The thermodynamic quantities appearing in the $f_0(\cdot)$ are T -
 429 temperature, μ_B - baryon chemical potential, μ_{I_3} - isospin chemical potential, μ_S
 430 - strange chemical potential, μ_C - charmed chemical potential and the s is a spin of
 431 a particle. The hydrodynamic calculations yield the flow velocity at freeze-out as
 432 well as the stress and bulk viscosity tensors required to calculate non-equilibrium
 433 corrections to the momentum distribution used in Eq. 2.7. The term coming from
 434 shear viscosity has a form [22]

$$\delta f_{shear} = f_0(1 \pm f_0) \frac{1}{2T^2(e + p)} p^\mu p^\nu \pi_{\mu\nu} \quad (2.11)$$

435 and bulk viscosity

$$\delta f_{bulk} = C f_0(1 \pm f_0) \left(\frac{(u^\mu p_\mu)^2}{3u^\mu p_\mu} - c_s^2 u^\mu p_\mu \right) \Pi \quad (2.12)$$

436 where c_s is sound velocity and

$$\frac{1}{C} = \frac{1}{3} \frac{1}{(2\pi)^3} \sum_{hadrons} \int d^3p \frac{m^2}{E} f_0(1 \pm f_0) \left(\frac{p^2}{3E} - c_s^2 E \right). \quad (2.13)$$

437 The equations presented above are directly used in the THERMINATOR to gen-
 438 erate the primordial hadrons (created during freeze-out) with the Monte-Carlo
 439 method. Resonances produced in this way, propagate and decay, in cascades if
 440 necessary. For every generated particle, its origin point either on a hypersurface
 441 or is associated with the point of the decay of the parent particle. This informa-
 442 tion is kept in the simulation due to its importance for the femtoscopic analysis.

⁴⁴³ **Chapter 3**

⁴⁴⁴ **Particle interferometry**

⁴⁴⁵ Two-particle interferometry (also called *femtoscopy*) gives a possibility to
⁴⁴⁶ investigate space-time characteristics of the particle-emitting source created
⁴⁴⁷ in heavy ion collisions. Through the study of particle correlations, their
⁴⁴⁸ momentum distributions can be used to obtain information about the spatial
⁴⁴⁹ extent of the created system. Using this method, one can measure sizes of the
⁴⁵⁰ order of 10^{-15} m and time of the order of 10^{-23} s.

⁴⁵¹ **3.1 HBT interferometry**

⁴⁵² In the 1956 Robert Hanbury Brown and Richard Q. Twiss proposed a
⁴⁵³ method which through analysis of interference between photons allowed to
⁴⁵⁴ investigate angular dimensions of stars. The most important result from the
⁴⁵⁵ Hanbury-Brown-Twiss experiments is that two indistinguishable particles can
⁴⁵⁶ produce an interference effect. There is almost no difference between normal
⁴⁵⁷ interferometry and HBT method, except that the latter one does not take into
⁴⁵⁸ account information about phase shift of registered particles. At the beginning
⁴⁵⁹ this method was used in astronomy for photon interference, but this effect can
⁴⁶⁰ be used also to measure extent of any emitting source. This method was adapted
⁴⁶¹ to heavy ion collisions to investigate dimensions of a system created in those
⁴⁶² collisions by studying correlations of identical particles [25]. The main difference
⁴⁶³ between HBT method in astronomy and femtoscopy is that the first one is based
⁴⁶⁴ on space-time HBT correlations and the latter one uses momentum correlations.
⁴⁶⁵ The momentum correlations yield the space-time picture of the source, whereas
⁴⁶⁶ the space-time HBT correlations provide the characteristic relative momenta of
⁴⁶⁷ emitted photons, which gives the angular size of the star without the knowledge
⁴⁶⁸ of its radius and lifetime [10].

469 3.2 Theoretical approach

470 Intensity interferometry in heavy ion physics uses similar mathematical form-
 471 alism as the astronomy HBT measurement. Through the measurement of corre-
 472 lation between particles as a function of their relative momentum one can deduce
 473 the average separation between emitting sources.

474 3.2.1 Conventions used

475 In heavy ion collisions to describe particular directions, components of mo-
 476 mentum and location of particles, one uses naming convention called the Bertsch-
 Pratt coordinate system. This system is presented in the Fig. 3.1. The three dir-

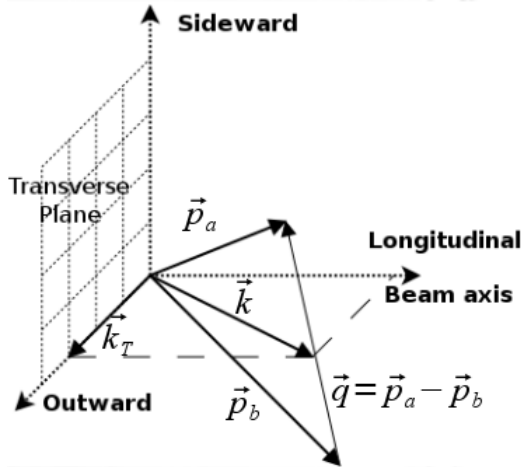


Figure 3.1: Bertsch-Pratt direction naming convention used in heavy ion collision.

477 ections are called *longitudinal*, *outward* and *sideward*. The longitudinal direction
 478 is parallel to the beam axis. The plane perpendicular to the beam axis is called
 479 a *transverse plane*. A projection of a particle pair momentum $\mathbf{k} = (\mathbf{p}_a + \mathbf{p}_b)/2$
 480 on a transverse plane (a *transverse momentum* \mathbf{k}_T) determines *outward* direction:
 481 $(\mathbf{k})_{out} = \mathbf{k}_T$. A direction perpendicular to the longitudinal and outward is called
 482 *sideward*.

483 A particle pair is usually described using two coordinate systems. The first
 484 one, *Longitudinally Co-Moving System* (**LCMS**) is moving along the particle pair
 485 with the longitudinal direction, in other words, the pair longitudinal momentum
 486 vanishes: $(\mathbf{p}_a)_{long} = -(\mathbf{p}_b)_{long}$. The second system is called *Pair Rest Frame* (**PRF**).
 487 In the PRF the centre of mass rests: $\mathbf{p}_a = -\mathbf{p}_b$. Variables which are expressed in
 488 the PRF are marked with a star (e.g. \mathbf{k}^*).

489 The transition of space-time coordinates from LCMS to PRF is simply
 a boost along the outward direction, with the transverse velocity of the

pair $\beta_T = (\mathbf{v}/c)_{out}$ [25]:

$$r_{out}^* = \gamma_t(r_{out} - \beta_T \Delta t) \quad (3.1)$$

$$r_{side}^* = r_{side} \quad (3.2)$$

$$r_{long}^* = r_{long} \quad (3.3)$$

$$\Delta t^* = \gamma_T(\Delta t - \beta_T r_{out}) , \quad (3.4)$$

where $\gamma_T = (1 - \beta_T^2)^{-1/2}$ is the Lorentz factor. However, in calculations performed in this work the equal time approximation is used, which assumes that particles in a pair were produced at the same time in PRF - the Δt^* is neglected.

The most important variables used to describe particle pair are their total momentum $\mathbf{P} = \mathbf{p}_a + \mathbf{p}_b$ and relative momentum $\mathbf{q} = \mathbf{p}_a - \mathbf{p}_b$. In the PRF one has $\mathbf{q} = 2\mathbf{k}^*$, where \mathbf{k}^* is a momentum of the first particle in PRF.

3.2.2 Two particle wave function

Let us consider two identical particles with momenta \mathbf{p}_1 and \mathbf{p}_2 emitted from space points \mathbf{x}_1 and \mathbf{x}_2 . Those emitted particles can be treated as two incoherent waves. If the particles are identical, they are also indistinguishable, therefore one

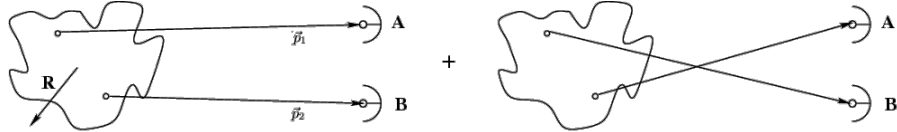


Figure 3.2: The pair wave function is a superposition of all possible states. In case of particle interferometry it includes two cases: particles with momenta p_1, p_2 registered by detectors A, B and p_1, p_2 registered by B, A respectively.

has also take into account the scenario, where the particle with momentum \mathbf{p}_1 is emitted from \mathbf{x}_2 and particle \mathbf{p}_2 from \mathbf{x}_1 (Fig. 3.2). In such case, the wave function describing behaviour of a pair has to contain both components [8]:

$$\Psi_{ab}(\mathbf{q}) = \frac{1}{\sqrt{2}} [\exp(-i\mathbf{p}_1\mathbf{x}_1 - i\mathbf{p}_2\mathbf{x}_2) \pm \exp(-i\mathbf{p}_2\mathbf{x}_1 - i\mathbf{p}_1\mathbf{x}_2)] . \quad (3.5)$$

A two particle wave function of identical bosons is symmetric ("+" sign in Eq. 3.5) and in case of identical fermions - antisymmetric ("−" sign). This anti-symmetrization or symmetrization implies the correlation effect coming from the Fermi-Dirac or Bose-Einstein statistics accordingly.

To provide full description of a system consisting of two charged hadrons, one has to include in the wave function besides quantum statistics also Coulomb and strong Final State Interactions. Considering identical particles systems, the quantum statistics is a main source of a correlation. Hence, in case of space-time analysis of particle emitting source, effects coming from the Coulomb and Strong interactions can be neglected.

513 **3.2.3 Source emission function**

514 To describe particle emitting source, one uses a single emission function [25]:

515

$$S_A(\mathbf{x}_1, \mathbf{p}_1) = \int S(\mathbf{x}_1, \mathbf{p}_1, \mathbf{x}_2, \mathbf{p}_2, \dots, \mathbf{x}_N, \mathbf{p}_N) d\mathbf{x}_2 d\mathbf{p}_2 \dots d\mathbf{x}_N d\mathbf{p}_N \quad (3.6)$$

516 and a two-particle one:

$$S_{AB}(\mathbf{x}_1, \mathbf{p}_1, \mathbf{x}_2, \mathbf{p}_2) = \int S(\mathbf{x}_1, \mathbf{p}_1, \mathbf{x}_2, \mathbf{p}_2, \dots, \mathbf{x}_N, \mathbf{p}_N) d\mathbf{x}_3 d\mathbf{p}_3 \dots d\mathbf{x}_N d\mathbf{p}_N . \quad (3.7)$$

517 Emission function $S(\cdot)$ can be interpreted as a probability to emit a particle, or
 518 a pair of particles from a given space-time point with a given momentum. In
 519 principle, the source emission function should encode all physics aspects of the
 520 particle emission process i.e. the symmetrization for bosons and fermions, as
 521 well as the two-body and many body Final State Interactions. Instead of this,
 522 one assume that each particle's emission process is independent - the interac-
 523 tion between final-state particles after their creation is independent from their
 524 emission process. The assumption of this independence allows to construct two-
 525 particle emission function from single particle emission functions via a convolu-
 526 tion [25]:

$$S(\mathbf{k}^*, \mathbf{r}^*) = \int S_A(\mathbf{p}_1, \mathbf{x}_1) S_B(\mathbf{p}_2, \mathbf{x}_2) \delta \left[\mathbf{k}^* - \frac{\mathbf{p}_1 + \mathbf{p}_2}{2} \right] \delta [\mathbf{r}^* - (\mathbf{x}_1 + \mathbf{x}_2)] \times d^4 \mathbf{x}_1 d^4 \mathbf{x}_2 d^4 \mathbf{x}_1 d^3 \mathbf{p}_1 d^3 \mathbf{p}_2 \quad (3.8)$$

527 In case of identical particles, ($S_A = S_B$) several simplifications can be made.
 528 A convolution of the two same Gaussian distributions is also a Gaussian distri-
 529 bution with σ multiplied by $\sqrt{2}$. Femtoscopy can give information only about
 530 two-particle emission function, but when considering Gaussian distribution as
 531 a source function in Eq. 3.8, one can obtain a σ of a single emission function
 532 from a two-particle emission function. The Eq. 3.8 is not reversible - an inform-
 533 ation about $S_A(\cdot)$ cannot be derived from $S_{AB}(\cdot)$. An exception from this rule
 534 is a Gaussian source function, hence it is often used in femtoscopic calculations.
 535 Considering pairs of identical particles, an emission function is assumed to be
 536 described by the following equation in the Pair Rest Frame [25]:

$$S_{1D}^{PRF}(\mathbf{r}^*) = \exp \left(-\frac{r_{out}^{*2} + r_{side}^{*2} + r_{long}^{*2}}{4R_{inv}^2} \right) . \quad (3.9)$$

To change from the three-dimensional variables to the one-dimensional variable
 one requires introduction of the proper Jacobian r^{*2} .

$$S_{1D}^{PRF}(r^*) = r^{*2} \exp \left(-\frac{r^{*2}}{4R_{inv}^2} \right) . \quad (3.10)$$

537 The “4” in the denominator before the “standard deviation” R_{inv} in the Gaussian
 538 distribution comes from the convolution of the two Gaussian distributions,
 539 which multiplies the R_{inv} by a factor of $\sqrt{2}$.

A more complex form of emission function was used by all RHIC and SPS experiments in identical pion femtoscopy:

$$S_{3D}^{LCMS}(\mathbf{r}) = \exp \left(-\frac{r_{out}^2}{4R_{out}^2} - \frac{r_{side}^2}{4R_{side}^2} - \frac{r_{long}^2}{4R_{long}^2} \right). \quad (3.11)$$

540 The main difference of this source function is that it has three different and independent widths R_{out} , R_{side} , R_{long} and they are defined in the LCMS, not in PRF.
 541 Unlike in PRF, in LCMS an equal-time approximation is not used. For identical
 542 particles this is not a problem - only Coulomb interaction inside a wave function
 543 depends on Δt .

544 Relationship between one-dimensional and three-dimensional source sizes

545 Up to now, most of femtoscopic measurements were limited only to averaged
 546 source size R_{av}^L (the letter “L” in superscript stands for LCMS):

$$S_{1D}^{LCMS}(\mathbf{r}) = \exp \left(-\frac{r_{out}^2 + r_{side}^2 + r_{long}^2}{2R_{av}^L} \right). \quad (3.12)$$

547 The relationship between between $S_{1D}^{LCMS}(\cdot)$ and $S_{3D}^{LCMS}(\cdot)$ is given by:

$$S_{3D}^{LCMS}(r) = \int \exp \left(-\frac{r_{out}^2}{2R_{out}^L} - \frac{r_{side}^2}{2R_{side}^L} - \frac{r_{long}^2}{2R_{long}^L} \right) \times \delta \left(r - \sqrt{r_{out}^2 + r_{side}^2 + r_{long}^2} \right) dr_{out} dr_{side} dr_{long}. \quad (3.13)$$

548 The one-dimensional source size corresponding to the three-dimensional one can
 549 be approximated by the following form:

$$S_{1D}^{LCMS}(r) = r^2 \exp \left(-\frac{r^2}{2R_{av}^L} \right). \quad (3.14)$$

550 The equation above assumes that $R_{out}^L = R_{side}^L = R_{long}^L$ hence $R_{av}^L = R_{out}^L$. If this
 551 condition is not satisfied, one can not give explicit mathematical relation between
 552 one-dimensional and three-dimensional source sizes. However, for realistic val-
 553 ues of R (i.e. for similar values of R_{out} , R_{side} , R_{long}), the S_{3D}^{LCMS} from Eq. 3.13 is
 554 not very different from Gaussian distribution and can be well approximated by
 555 Eq. 3.13.

556 A deformation of an averaged source function in case of big differences in
 557 R_{out} , R_{side} , R_{long} is presented in the Fig. 3.3. A three-dimensional Gaussian dis-
 558 tribution with varying widths was averaged into one-dimensional function using
 559

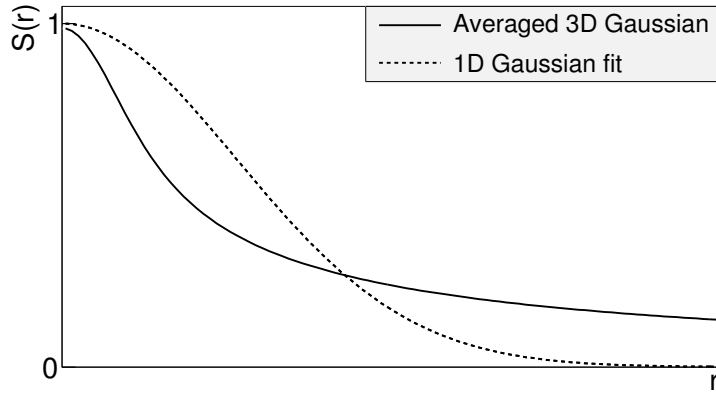


Figure 3.3: An averaged three-dimensional Gaussian source function with different widths was averaged into one-dimensional function. To illustrate deformations, one-dimensional Gaussian distribution was fitted.

the Eq. 3.13. Afterwards, an one-dimensional Gaussian distribution was fitted. One can notice a heavy tail of an averaged distribution in long r region, which makes an approximation using one-dimensional distribution in this case quite inaccurate.

Using Eq. 3.13 and Eq. 3.14 one can obtain a relation between one-dimensional width and the three-dimensional ones. Through numerical calculations one can find the following approximate relation [25]:

$$R_{av}^L = \sqrt{\left(R_{out}^L\right)^2 + \left(R_{side}^L\right)^2 + \left(R_{long}^L\right)^2} / 3 . \quad (3.15)$$

This equation does not depend on the pair velocity, hence it is valid in the LCMS and PRF.

3.2.4 Theoretical correlation function

The fundamental object in a particle interferometry is a correlation function. The correlation function is defined as:

$$C(\mathbf{p}_a, \mathbf{p}_b) = \frac{P_2(\mathbf{p}_a, \mathbf{p}_b)}{P_1(\mathbf{p}_a)P_1(\mathbf{p}_b)} , \quad (3.16)$$

where P_2 is a conditional probability to observe a particle with momentum \mathbf{p}_b if particle with momentum \mathbf{p}_a was also observed. A P_1 is a probability to observe a particle with a given momentum. The relationship between source emission function, pair wave function and the correlation function is described by the following equation:

$$C(\mathbf{p}_1, \mathbf{p}_2) = \int S_{AB}(\mathbf{p}_1, \mathbf{x}_1, \mathbf{p}_2, \mathbf{x}_2) |\Psi_{AB}|^2 d^4\mathbf{x}_1 d^4\mathbf{x}_2 \quad (3.17)$$

Substituting the one-dimensional emission function (Eq. 3.10) into the integral above yields the following form of correlation function in PRF:

$$C(q) = 1 + \lambda \exp(-R_{inv}^2 q^2) \quad (3.18)$$

where q is a momentum difference between two particles. When using the three-dimensional emission function (Eq. 3.11) one gets the following correlation function defined in the LCMS:

$$C(\mathbf{q}) = 1 + \lambda \exp(-R_{out}^2 q_{out}^2 - R_{side}^2 q_{side}^2 - R_{long}^2 q_{long}^2) \quad (3.19)$$

574 where q_{out} , q_{side} , q_{long} are \mathbf{q} components in the outward, sideward and longitudinal direction. The λ parameter in the equations above determines correlation
 575 strength. The lambda parameter has values in the range $\lambda \in [-0.5, 1]$ and it depends on a pair type. In case of pairs of identical bosons (like $\pi\pi$ or KK) the
 576 lambda parameter $\lambda \rightarrow 1$. For identical fermions (e.g. $p-p$) $\lambda \rightarrow -0.5$. Values of
 577 λ observed experimentally are lower than 1 (for bosons) and greater than -0.5
 578 (for fermions). There are few explanations to this effect: detector efficiencies,
 579 inclusion of misidentified particles in a used sample or inclusion of non-correlated
 580 pairs (when one or both particles come from e.g. long-lived resonance). The
 581 analysis carried out in this work uses data from a model, therefore the detector
 582 efficiency and particle purity is not taken into account [25].
 583

584 3.2.5 Spherical harmonics decomposition of a correlation function

585 Results coming from an analysis using three-dimensional correlation function
 586 in Cartesian coordinates are quite difficult to visualize. To do that, one usually
 587 performs a projection into a one dimension in outward, sideward and longitudinal
 588 directions. One may loose important information about a correlation
 589 function in this procedure, because it gives only a limited view of the full three-
 590 dimensional structure. Recently, a more advanced way of presenting correlation
 591 function - a spherical harmonics decomposition, was proposed. The three-
 592 dimensional correlation function is decomposed into an infinite set of components
 593 in a form of one-dimensional histograms $C_l^m(q)$. In this form, a correlation
 594 function is defined as a sum of a series [26]:
 595

$$C(\mathbf{q}) = \sum_{l,m} C_l^m(q) Y_l^m(\theta, \phi), \quad (3.20)$$

596 where $Y_l^m(\theta, \phi)$ is a spherical harmonic function. Spherical harmonics are an
 597 orthogonal set of solutions to the Laplace's equation in spherical coordinates
 598 Hence, in this approach, a correlation function is defined as a function of q , θ
 599 and ϕ . To obtain C_l^m coefficients in the series, one has to calculate the following
 600 integral:

$$C_l^m(q) = \int_{\Omega} C(q, \theta, \phi) Y_l^m(\theta, \phi) d\Omega, \quad (3.21)$$

601 where Ω is a full solid angle.

Spherical harmonics representation has several important advantages. The main advantage of this decomposition is that it requires less statistics than traditional analysis performed in Cartesian coordinates. Another one is that it encodes full three-dimensional information in a set of one-dimensional plots. In principle it does not have to be an advantage, because full description of a correlation function requires infinite number of l, m components. But it so happens that the intrinsic symmetries of a pair distribution in a femtoscopic analysis result in most of the components to vanish. For the identical particles correlation functions, all coefficients with odd values of l and m disappear. It has also been shown, that the most significant portion of femtoscopic data is stored in the components with the lowest l values. It is expected that, the main femtoscopic information is contained in the following components [25]:

$$C_0^0 \rightarrow R_{LCMS}, \quad (3.22)$$

$$\Re C_2^0 \rightarrow \frac{R_T}{R_{long}}, \quad (3.23)$$

$$\Re C_2^2 \rightarrow \frac{R_{out}}{R_{side}}, \quad (3.24)$$

602 where $R_{LCMS} = \sqrt{(R_{out}^2 + R_{side}^2 + R_{long}^2)/3}$ and $R_T = \sqrt{(R_{out}^2 + R_{side}^2)/2}$.
 603 The C_0^0 is sensitive to the overall size of a correlation function. The $\Re C_2^0$ carries
 604 the information about the ratio of the transverse to the longitudinal radii, due
 605 to its $\cos^2(\theta)$ weighting in Y_2^0 . The component $\Re C_2^2$ with its $\cos^2(\phi)$ weighting
 606 encodes the ratio between outward and sideward radii. Thus, the spherical har-
 607 monics method allows to obtain and analyze full three-dimensional femtoscopic
 608 information from a correlation function [25].

609 3.3 Experimental approach

610 The correlation function is defined as a probability to observe two particles
 611 together divided by the product of probabilities to observe each of them sepa-
 612 rately (Eq. 3.16). Experimentally this is achieved by dividing two distributions
 613 of relative momentum of pairs of particles coming from the same event and the
 614 equivalent distribution of pairs where each particle is taken from different colli-
 615 sions. In this way, one obtains not only femtoscopic information but also all other
 616 event-wide correlations. This method is useful for experimentalists to estimate
 617 the magnitude of non-femtoscopic effects. There exists also a different approach,
 618 where two particles in pairs in the second distribution are also taken from the
 619 same event. The second method gives only information about physical effects
 620 accessible via femtoscopy. The aim of this work is a study of effects coming from
 621 two particle interferometry, hence the latter method was used.

622 In order to calculate experimental correlation function, one uses the follow-
 623 ing approach. One has to construct two histograms: the *numerator* N and the

624 denominator D with the particle pairs momenta, where particles are coming from
 625 the same event. Those histograms can be one-dimensional (as a function of $|\mathbf{q}|$),
 626 three dimensional (a function of three components of \mathbf{q} in LCMS) or a set of one-
 627 dimensional histogram representing components of the spherical harmonic de-
 628 composition of the distribution. The second histogram, D is filled for each pair
 629 with the weight 1.0 at a corresponding relative momentum $\mathbf{q} = 2\mathbf{k}^*$. The first one,
 630 N is filled with the same procedure, but the weight is calculated as $|\Psi_{ab}(\mathbf{r}^*, \mathbf{k}^*)|^2$.
 631 A division N/D gives the correlation function C . This procedure can be simply
 632 written as [25]:

$$C(\mathbf{k}^*) = \frac{N}{D} = \frac{\sum_{n_i \in D} \delta(\mathbf{k}^*_i - \mathbf{k}^*) |\Psi_{ab}(\mathbf{r}^*_i, \mathbf{k}^*_i)|^2}{\sum_{n_i \in D} \delta(\mathbf{k}^*_i - \mathbf{k}^*)} . \quad (3.25)$$

The D histogram represents the set of all particle pairs used in calculations.
 The n_i is a pair with the its relative momentum \mathbf{k}^*_i and relative separation \mathbf{r}^*_i .
 The wave function used in Eq. 3.25 has one of the following forms:

$$|\Psi_{\pi\pi}(\mathbf{r}^*, \mathbf{k}^*)|^2 = |\Psi_{KK}(\mathbf{r}^*, \mathbf{k}^*)|^2 = 1 + \cos(2\mathbf{k}^*\mathbf{r}^*) , \quad (3.26)$$

$$|\Psi_{pp}(\mathbf{r}^*, \mathbf{k}^*)|^2 = 1 - \frac{1}{2} \cos(2\mathbf{k}^*\mathbf{r}^*) . \quad (3.27)$$

633 The first one is used in case of bosons, and the latter one is for identical fermi-
 634 ons. Mathematically, the procedure of calculating the Eq. 3.25 is equivalent to a
 635 calculation of an integral in Eq. 3.17 through a Monte-Carlo method.

636 3.4 Scaling of femtoscopic radii

637 In the hydrodynamic models describing expansion of a quark-gluon plasma,
 638 particles are emitted from the source elements. Each of the source elements is
 639 moving with the velocity u_μ given by hydrodynamic equations. Because solu-
 640 tions of those equations are smooth, nearby source elements have similar velo-
 641 cities. Each emitted particle from a certain source element is boosted with the
 642 flow velocity u_μ according to the point of origin. Hence particles emitted close
 643 to each other (pairs with large transverse momentum $|\mathbf{k}_T|$) will gain the similar
 644 velocity boost, they can combine into pairs with small relative momenta ($|\mathbf{q}|$) and
 645 therefore become correlated. If the two particles are emitted far away from each
 646 other (a pair with small $|\mathbf{k}_T|$), the flow field u_μ in their point of emission might
 647 be very different and it will be impossible for them to have sufficiently small rel-
 648 ative momenta in order to be in region of interference effect. This effect is visible
 649 in a width of a correlation function in the Fig. 3.4. The correlation function gets
 650 broader for greater values of $|\mathbf{k}_T|$ and the femtoscopic radius R becomes smal-
 651 ler [8, 27].

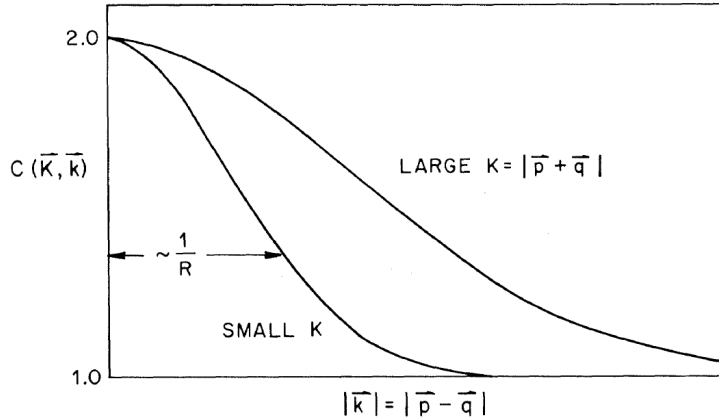


Figure 3.4: Correlation function width dependence on total pair momentum. Pion pairs with a large total momentum are more correlated [27].

652 3.4.1 Scaling in LCMS

Hydrodynamic calculations performed in LCMS show that femtoscopic radii in outward, sideward, and longitudinal direction show dependence on transverse mass $m_T = \sqrt{k_T^2 + m}$, where m is a mass of a particle [28]. Moreover, experimental results show that this scaling is observed for R_{LCMS} radii also. This dependence can be expressed as follows:

$$R_i = \alpha m_T^{-\beta} \quad (3.28)$$

653 where i subscript indicates that this equation applies to R_{out} , R_{side} and R_{long}
 654 radii. The β exponent is approximately equal 0.5. In case of strong transversal
 655 expansion of the emitting source, the decrease of longitudinal interferometry ra-
 656 dius can be more quick than $m_T^{-0.5}$, hence one can expect for longitudinal radii
 657 lower values of $\beta < 0.5$ [28].

658 3.4.2 Scaling in PRF

659 In the collisions at the LHC energies, pions are most abundant particles and
 660 their multiplicities are large enough to enable three-dimensional analysis. How-
 661 ever, for heavier particles, such as kaons and protons statistical limitations arise.
 662 Hence it is often possible to only measure one-dimensional radius R_{inv} for those
 663 particles. The R_{inv} is then calculated in the PRF. The transition from LCMS to
 664 PRF is a Lorentz boost in the direction of pair transverse momentum with velo-
 665 city $\beta_T = p_T/m_T$. Hence only R_{out} radius changes:

$$R_{out}^* = \gamma_T R_{out}. \quad (3.29)$$

666 The one-dimensional R_{inv} radius is direction-averaged source size in PRF. One
 667 can notice, that such power-law scaling of R_{inv} described by Eq. 3.28 is not

668 observed. To recover such scaling in PRF one has to take into consideration two
 669 effects when transforming variables from LCMS to PRF: overall radius growths
 670 and source distribution becomes non-Gaussian, while developing long-range
 671 tails (see Fig.3.3 for an example). The interplay of these two effects can be
 672 accounted with an approximate formula:

$$R_{inv} = \sqrt{(R_{out}^2 \sqrt{\gamma_T} + R_{side}^2 + R_{long}^2)/3} . \quad (3.30)$$

Assuming that all radii are equal $R_{out} = R_{side} = R_{long}$ this formula can be simplified:

$$R_{LCMS} \approx R_{inv} \times [(\sqrt{\gamma_T} + 2)/3]^{-1/2} . \quad (3.31)$$

673 This approximate formula allows to restore power-law behaviour of the scaled
 674 radii not only when the radii are equal, but also when their differences are small
 675 (for explanation see the last part of the section 3.2.3).

676 This method of recovering scaling in PRF can be used as a tool for the search
 677 of hydrodynamic collectivity between pions, kaons and protons in heavy ion col-
 678 lisions with the measurement of one-dimensional radius in PRF.

679 **Chapter 4**

680 **Results**

681 **4.1 Identical particles correlations**

682 **4.1.1 Spherical harmonics components**

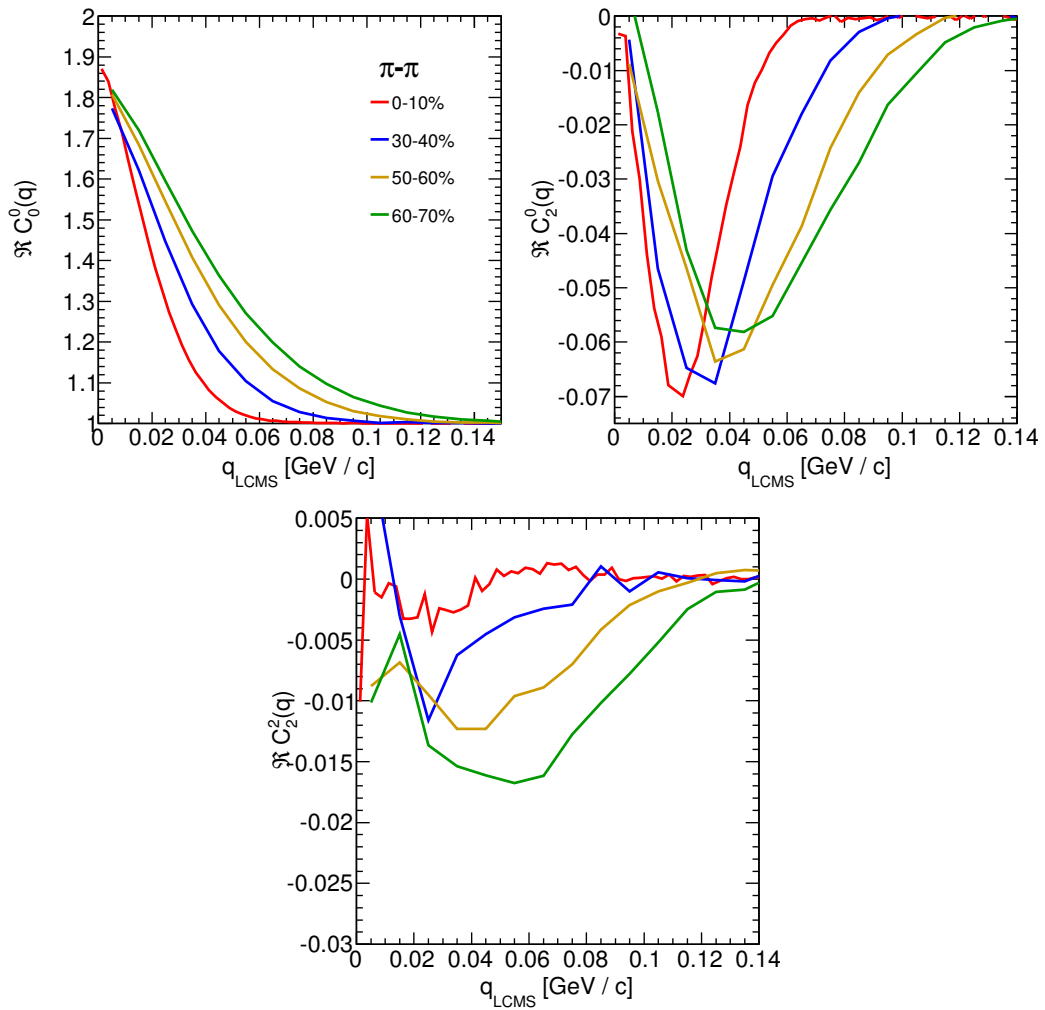


Figure 4.1: no caption

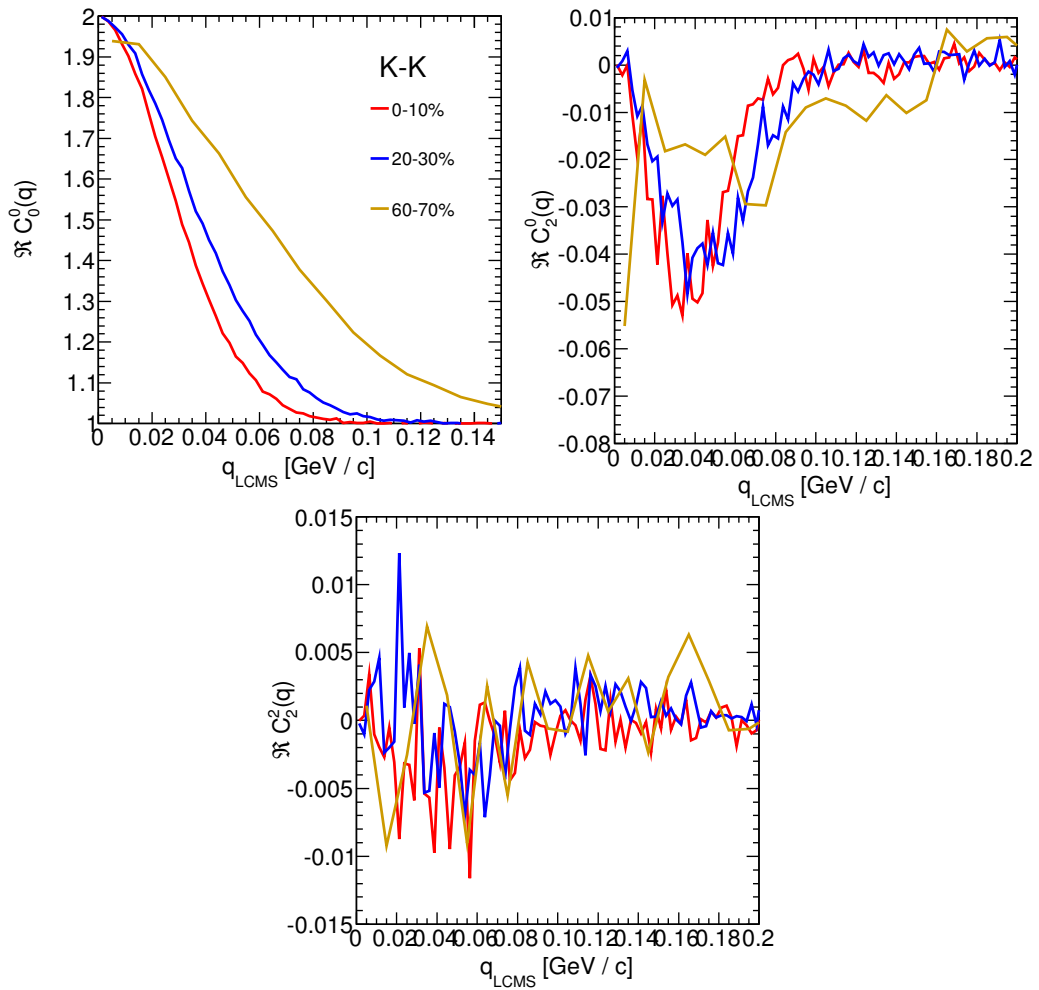


Figure 4.2: no caption

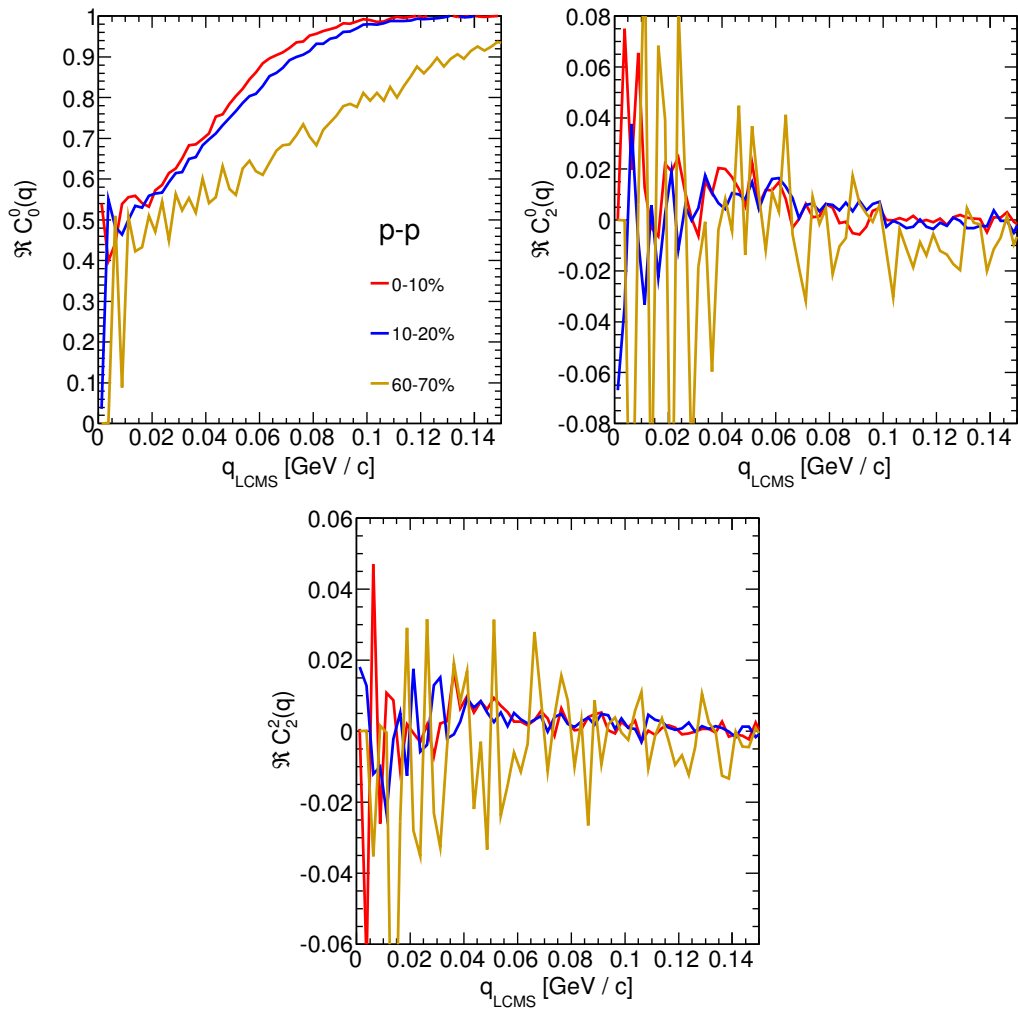


Figure 4.3: no caption

683 **4.1.2 Centrality dependence of a correlation function**

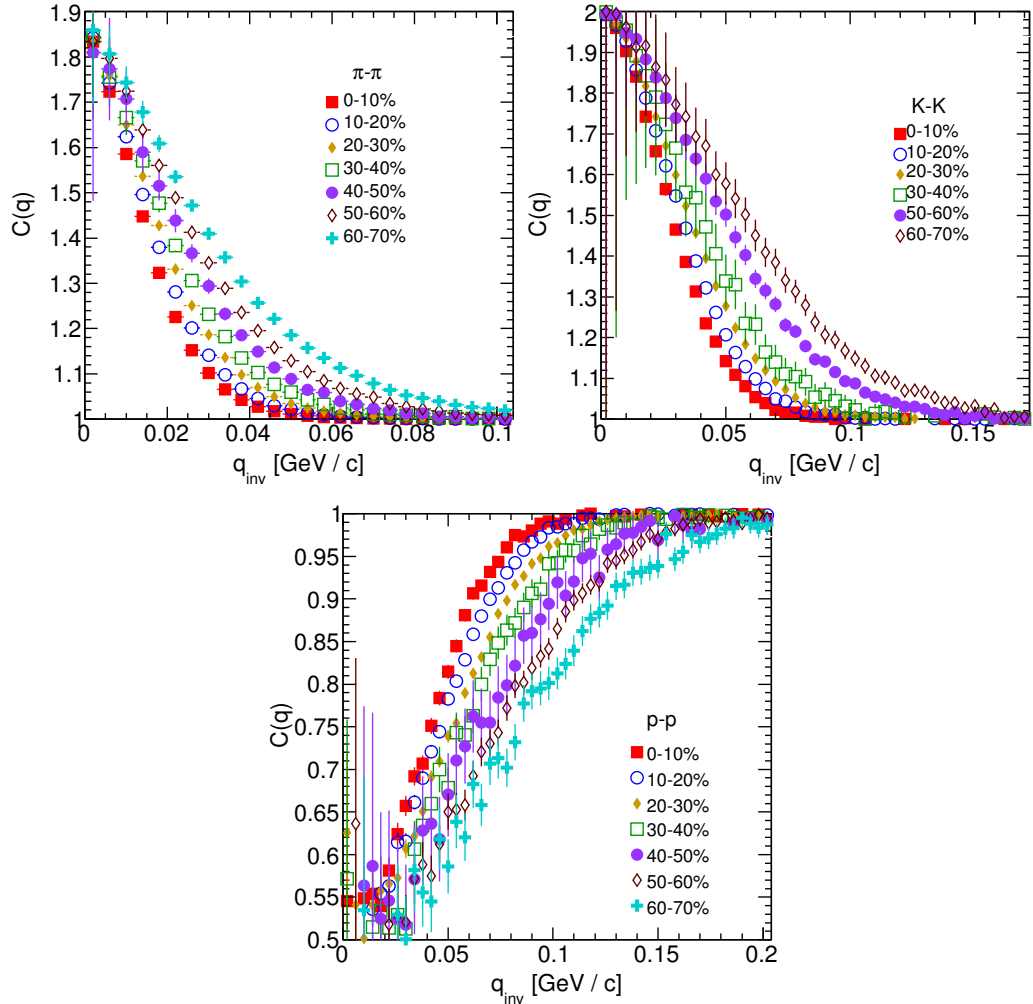


Figure 4.4: no caption

684 **4.1.3 k_T dependence of a correlation function**

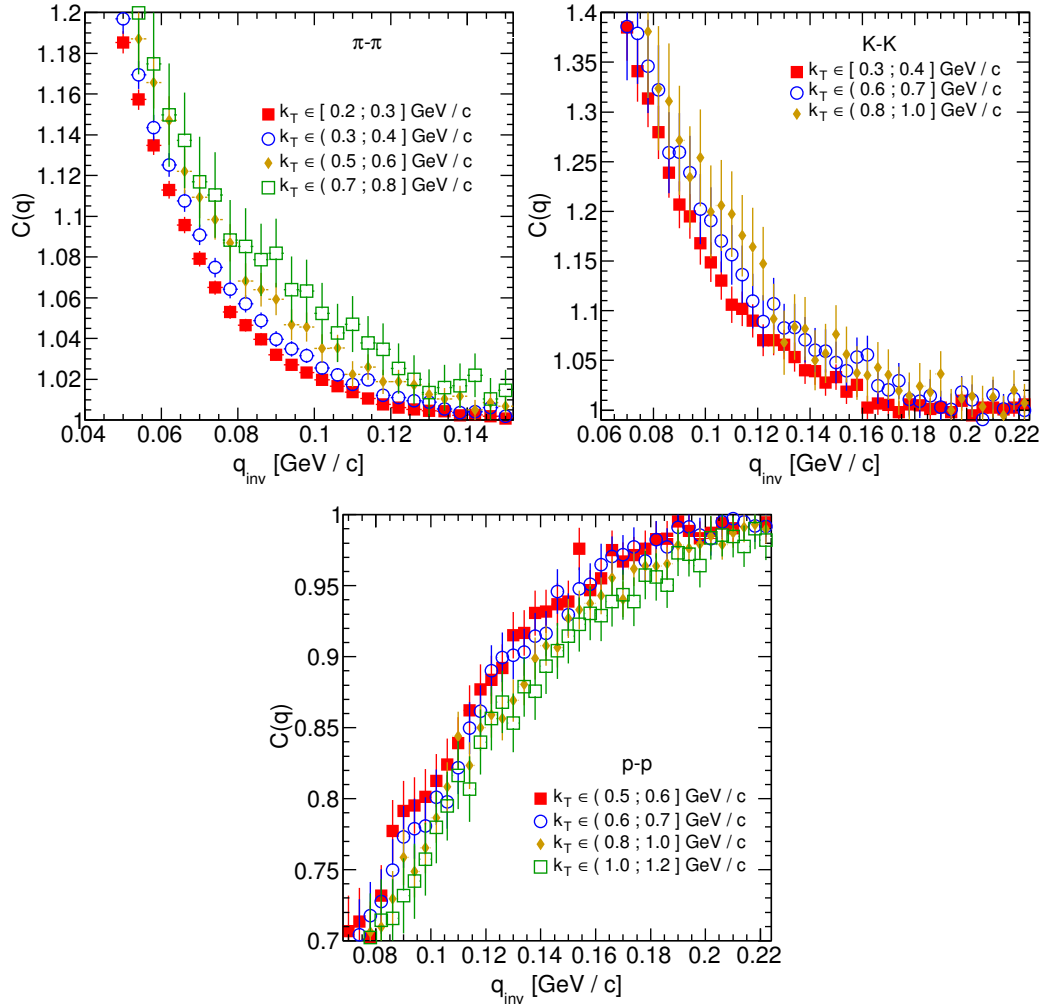


Figure 4.5: no caption

685 4.2 Results of the fitting procedure

686 4.2.1 Femtoscopic radii scaling with the transverse mass

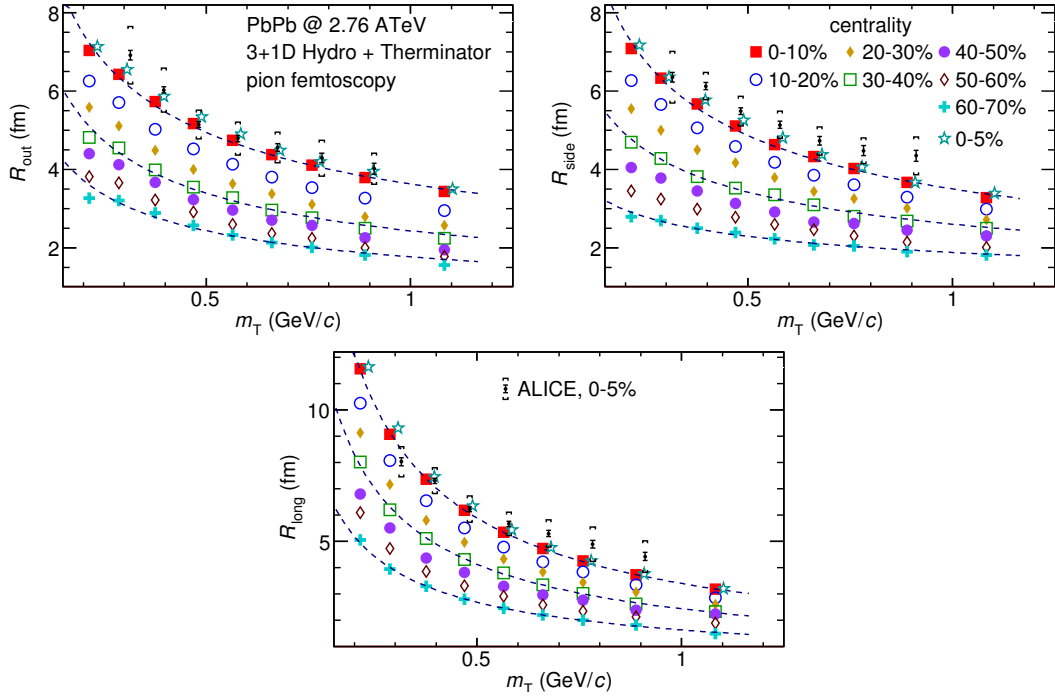


Figure 4.6: no caption [29] [30].

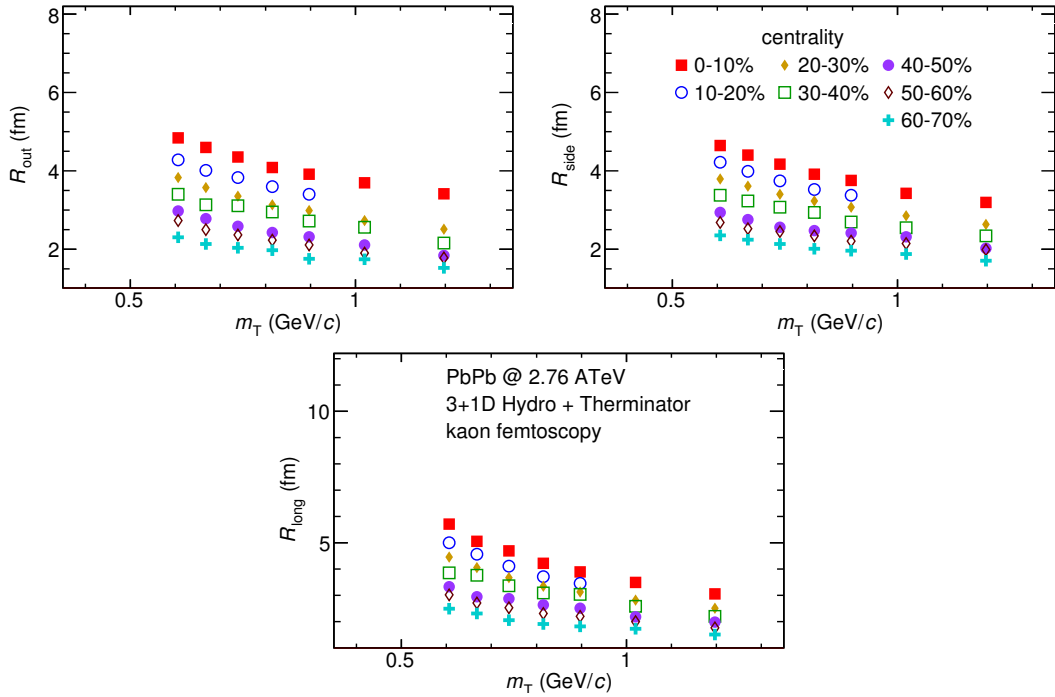


Figure 4.7: no caption [30].

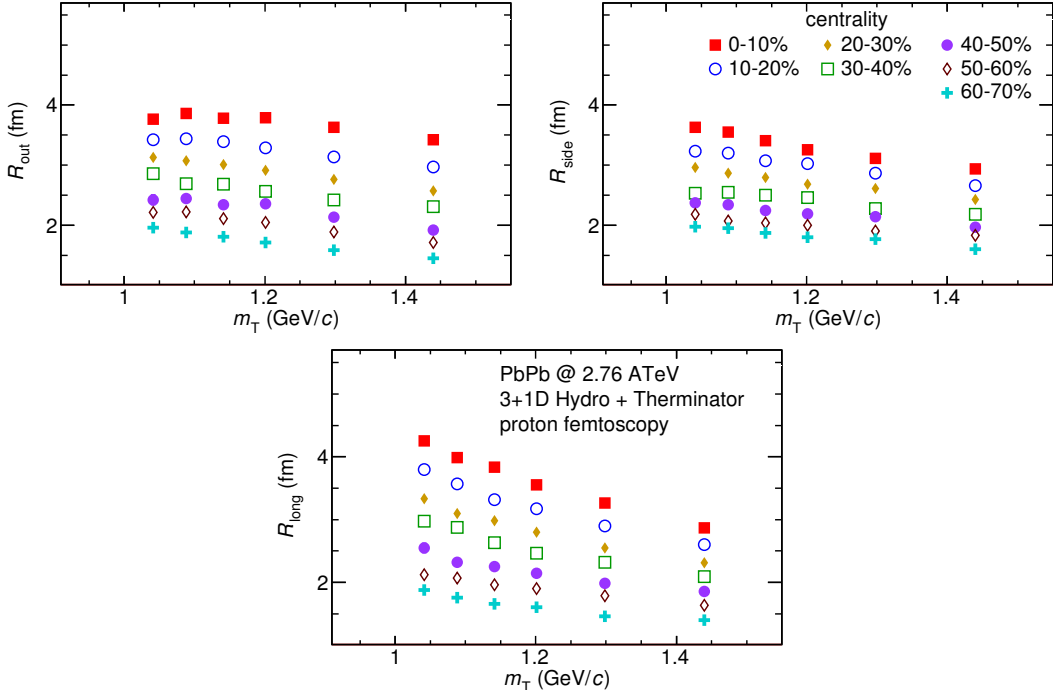


Figure 4.8: no caption [30].

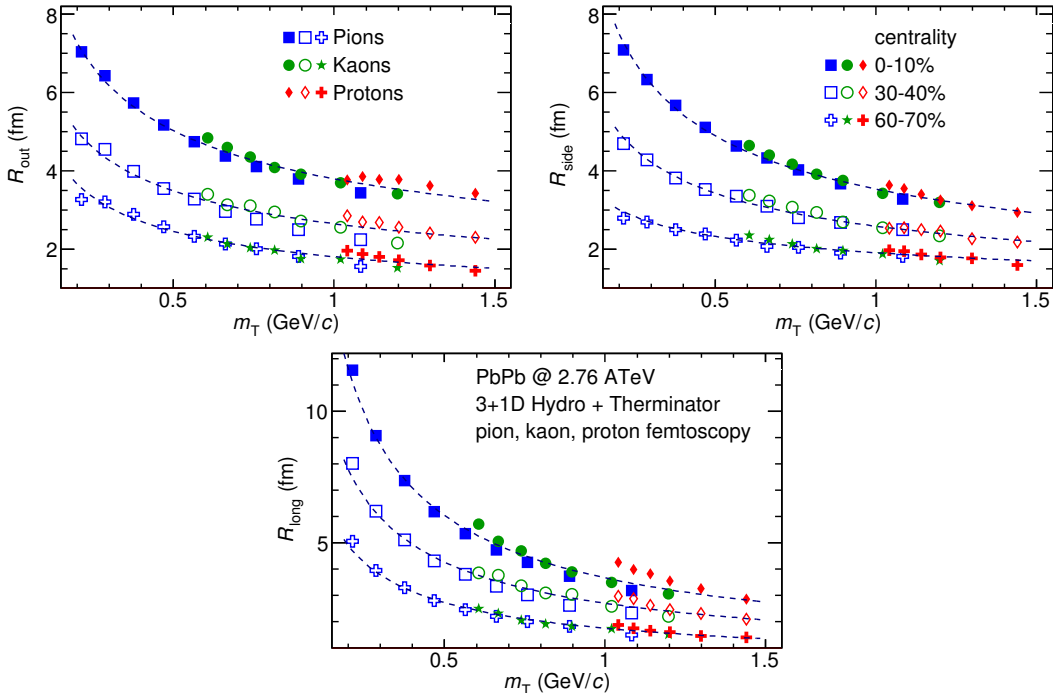


Figure 4.9: no caption [30].

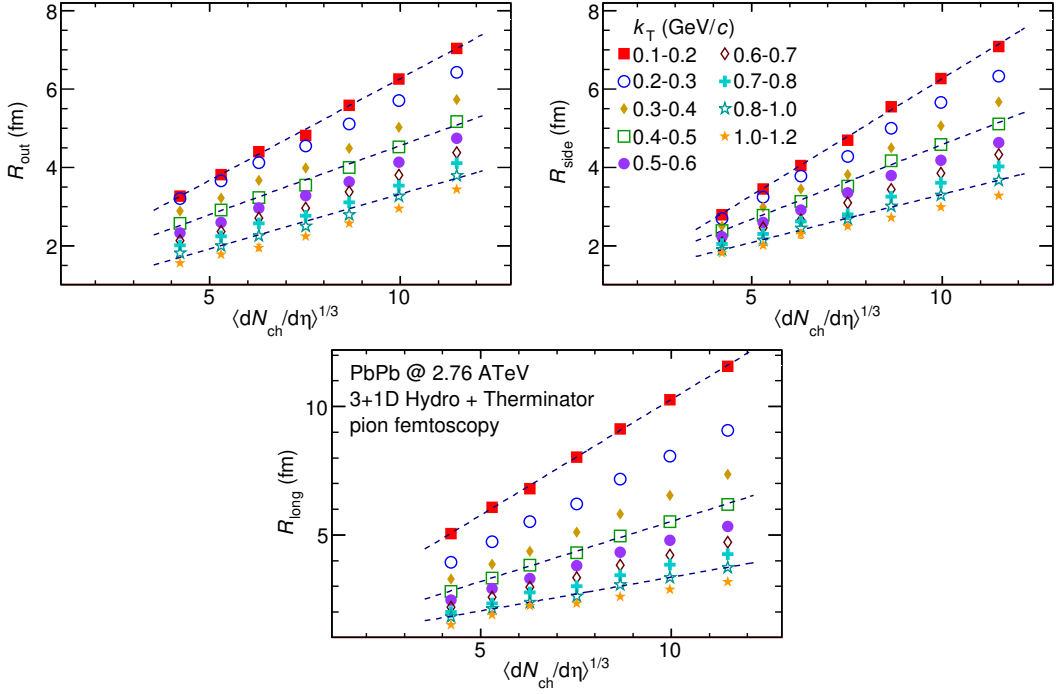


Figure 4.10: no caption [30].

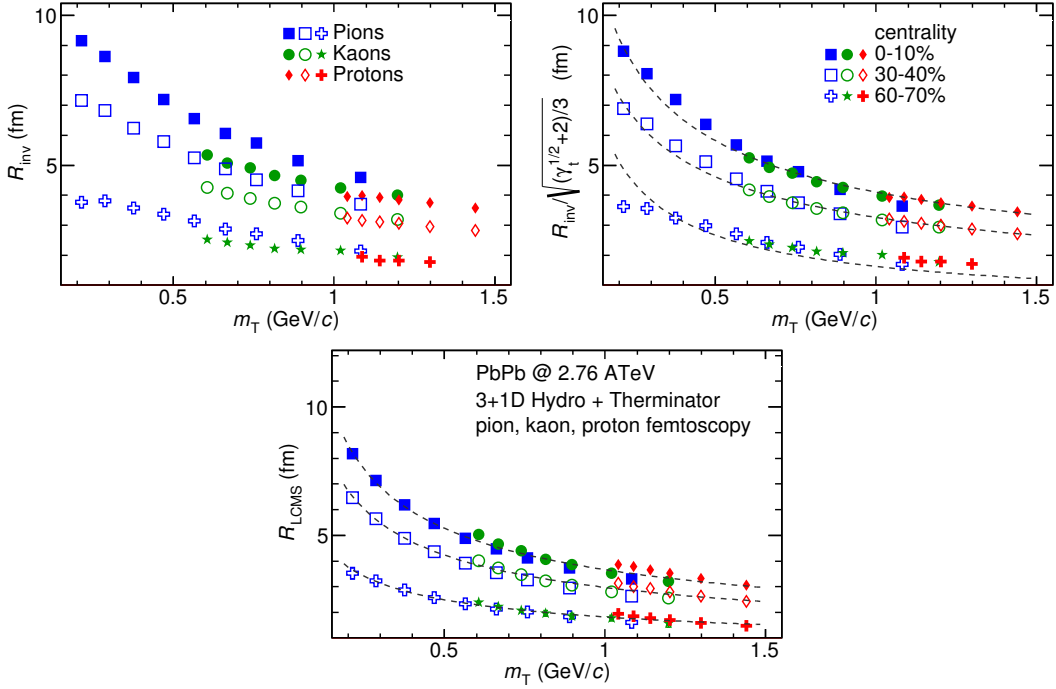


Figure 4.11: no caption [30].

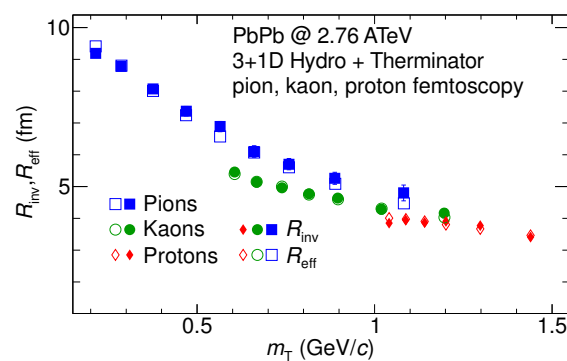


Figure 4.12: no caption [30].

⁶⁸⁷ **4.3 Discussion of results**

688 **Chapter 5**

689 **Summary**

690 Bibliography

- 691 [1] Standard Model of Elementary Paticles - Wikipedia, the free encyclopedia
692 http://en.wikipedia.org/wiki/standard_model.
- 693 [2] R. Aaij et al. (LHCb Collaboration). Observation of the resonant character of
694 the $z(4430)^-$ state. *Phys. Rev. Lett.*, 112:222002, Jun 2014.
- 695 [3] Donald H. Perkins. *Introduction to High Energy Physics*. Cambridge University Press,
696 fourth edition, 2000. Cambridge Books Online.
- 697 [4] G. Odyniec. *Phase Diagram of Quantum Chromo-Dynamics* - course at Faculty
698 of Physics, Warsaw University of Technology, Jun 2012.
- 699 [5] J. Beringer et al. (Particle Data Group). The Review of Particle Physics. *Phys.*
700 *Rev.*, D86:010001, 2012.
- 701 [6] Z. Fodor and S.D. Katz. The Phase diagram of quantum chromodynamics.
702 2009.
- 703 [7] F. Karsch. Lattice results on QCD thermodynamics. *Nuclear Physics A*, 698(1-
704 4):199 – 208, 2002.
- 705 [8] Adam Kisiel. *Studies of non-identical meson-meson correlations at low relative ve-*
706 *locities in relativistic heavy-ion collisions registered in the STAR experiment*. PhD
707 thesis, Warsaw University of Technology, Aug 2004.
- 708 [9] J. Bartke. *Relativistic Heavy Ion Physics*. World Scientific Pub., 2009.
- 709 [10] W. Florkowski. *Phenomenology of Ultra-Relativistic Heavy-Ion Collisions*.
710 World Scientific, 2010.
- 711 [11] Science Grid This Week, October 25, 2006 - Prob-
712 ing the Perfect Liquid with the STAR Grid
713 http://www.interactions.org/sgtw/2006/1025/star_grid_more.html.
- 714 [12] K. Grebieszkow. Fizyka zderzeń ciężkich jonów,
715 <http://www.if.pw.edu.pl/~kperl/hip/hip.html>.
- 716 [13] Ulrich W. Heinz. From SPS to RHIC: Maurice and the CERN heavy-ion
717 programme. *Phys.Scripta*, 78:028005, 2008.

- 718 [14] J. Adams et al. Identified particle distributions in pp and Au+Au collisions
719 at $s(\text{NN})^{**}(1/2) = 200 \text{ GeV}$. *Phys.Rev.Lett.*, 92:112301, 2004.
- 720 [15] G. David, R. Rapp, and Z. Xu. Electromagnetic Probes at RHIC-II. *Phys.Rept.*,
721 462:176–217, 2008.
- 722 [16] A. Marin et al. Dilepton measurements with CERES. *PoS*, CPOD07:034,
723 2007.
- 724 [17] J. Adams et al. Experimental and theoretical challenges in the search for the
725 quark gluon plasma: The STAR Collaboration’s critical assessment of the
726 evidence from RHIC collisions. *Nucl.Phys.*, A757:102–183, 2005.
- 727 [18] Adam Kisiel, Tomasz Taluc, Wojciech Broniowski, and Wojciech
728 Florkowski. THERMINATOR: THERMal heavy-IoN generATOR. *Comput.Phys.Commun.*, 174:669–687, 2006.
- 730 [19] Mikolaj Chojnacki, Adam Kisiel, Wojciech Florkowski, and Wojciech Bro-
731 niowski. THERMINATOR 2: THERMal heavy IoN generATOR 2. *Comput.Phys.Commun.*, 183:746–773, 2012.
- 733 [20] I. et al (BRAHMS Collaboration) Bearden. Charged meson rapidity distri-
734 butions in central Au + Au collisions at $\sqrt{s_{\text{NN}}} = 200 \text{ GeV}$. *Phys. Rev. Lett.*,
735 94:162301, Apr 2005.
- 736 [21] W. Israel and J.M. Stewart. Transient relativistic thermodynamics and kin-
737 etic theory. *Annals of Physics*, 118(2):341 – 372, 1979.
- 738 [22] Piotr Bożek. Flow and interferometry in (3 + 1)-dimensional viscous hydro-
739 dynamics. *Phys. Rev. C*, 85:034901, Mar 2012.
- 740 [23] K. Kovtun, P. D. T. Son, and A. O. Starinets. Viscosity in strongly interacting
741 quantum field theories from black hole physics. *Phys. Rev. Lett.*, 94:111601,
742 Mar 2005.
- 743 [24] Fred Cooper and Graham Frye. Single-particle distribution in the hydro-
744 dynamic and statistical thermodynamic models of multiparticle production.
745 *Phys. Rev. D*, 10:186–189, Jul 1974.
- 746 [25] Adam Kisiel. Nonidentical-particle femtoscopy at $\sqrt{s_{\text{NN}}} = 200 \text{ GeV}$ in hy-
747 drodynamics with statistical hadronization. *Phys. Rev. C*, 81:064906, Jun
748 2010.
- 749 [26] Adam Kisiel and David A. Brown. Efficient and robust calculation of femto-
750 scopic correlation functions in spherical harmonics directly from the raw
751 pairs measured in heavy-ion collisions. *Phys.Rev.*, C80:064911, 2009.
- 752 [27] S. Pratt. Pion Interferometry for Exploding Sources. *Phys.Rev.Lett.*, 53:1219–
753 1221, 1984.

- 754 [28] S.V. Akkelin and Yu.M. Sinyukov. The HBT-interferometry of expanding
755 inhomogeneous sources. *Z.Phys.*, C72:501–507, 1996.
- 756 [29] K. Aamodt et al. Two-pion Bose-Einstein correlations in central Pb-Pb colli-
757 sions at $\sqrt{s_{NN}} = 2.76$ TeV. *Phys.Lett.*, B696:328–337, 2011.
- 758 [30] A. Kisiel, M. Galazyn, and P. Bozek. Pion, kaon, and proton femtoscopy in
759 Pb–Pb collisions at $\sqrt{s_{NN}}=2.76$ TeV modeled in 3+1D hydrodynamics. 2014.

760 List of Figures

761 1.1	The Standard Model of elementary particles [1].	2
762 1.2	A string break and a creation of a pair quark-anti-quark [4].	4
763 1.3	The coupling parameter α_s dependence on four-momentum trans-	
764 1.4	fer Q^2 [5].	5
765 1.5	The QCD potential for a pair quark-antiquark as a function of dis-	
766 1.6	tance for different temperatures. A value of a potential decreases	
767 1.7	with the temperature [4].	5
768 1.8	A number of degrees of freedom as a function of a temperature [7].	6
769 1.9	1.6 Phase diagram coming from the Lattice QCD calculations [8]. . . .	7
770 1.7	1.7 Left: stages of a heavy ion collision simulated in the UrQMD	
771 1.8	model. Right: schematic view of a heavy ion collision evolution [8].	8
772 1.9	1.8 Overlapping region which is created in heavy ion collisions has an	
773 1.10	almond shape. Visible x-z plane is a <i>reaction plane</i> . The x-y plane is	
774 1.11	a <i>transverse plane</i> . The z is a direction of the beam [11].	10
775 1.10	1.9 Cross-section of a heavy ion collision in a transverse plane. Ψ_R	
776 1.11	is an angle between transverse plane and the reaction plane. The	
777 1.12	b parameter is an <i>impact parameter</i> - a distance between centers of	
778 1.13	nuclei during a collision. An impact parameter is related with the	
779 1.14	centrality of a collision and a volume of the quark-gluon plasma [12].	11
780 1.15	1.10 <i>Lower</i> : The elliptic flow v_2 follows the hydrodynamical predictions	
781 1.16	for an ideal fluid perfectly. Note that > 99% of all final hadrons	
782 1.17	have $p_T < 1.5$ GeV/c. <i>Upper left</i> : The v_2 plotted versus transverse	
783 1.18	kinetic energy $KE_T = m_T - m_0 = \sqrt{p_T^2 + m_0^2} - m_0$. The v_2 follows	
784 1.19	different universal curves for mesons and baryons. <i>Upper right</i> :	
785 1.20	When scaled by the number of valence quarks, the v_2 follows the	
786 1.21	same universal curve for all hadrons and for all values of scaled	
787 1.22	transverse kinetic energy [13].	12
788 1.23	1.11 Invariant yield of particles versus transverse mass	
789 1.24	$m_T = \sqrt{p_T^2 + m_0^2}$ for π^\pm , K^\pm , p and \bar{p} at mid-rapidity for p+p	
790 1.25	collisions (bottom) and Au+Au events from 70-80% (second	
791 1.26	bottom) to 0-5% (top) centrality [14].	13

792 1.12	Thermal photons spectra for the central Au+Au collisions at $\sqrt{s_{NN}} = 200$ GeV at computed within different hydrodynamical models compared with the pQCD calculations (solid line) and experimental data from PHENIX (black dots) [15].	14
793 1.13	Left: Invariant mass spectrum of e^+e^- pairs in Pb+Au collisions at 158A GeV compared to the sum coming from the hadron decays predictions. Right: The expectations coming from model calculations assuming a dropping of the ρ mass (blue) or a spread of the ρ width in the medium (red) [16].	15
794 1.14	Azimuthal angle difference $\Delta\phi$ distributions for different colliding systems at $\sqrt{s_{NN}} = 200$ GeV. Transverse momentum cut: $p_T > 2$ GeV. For the Au+Au collisions the away-side jet is missing [17]. . .	16
801 3.1	Bertsch-Pratt direction naming convention used in heavy ion collision.	22
802 3.2	The pair wave function is a superposition of all possible states. In case of particle interferometry it includes two cases: particles with momenta p_1, p_2 registered by detectors A, B and p_1, p_2 registered by B, A respectively.	23
803 3.3	An averaged three-dimensional Gaussian source function with different widths was averaged into one-dimensional function. To illustrate deformations, one-dimensional Gaussian distribution was fitted.	26
804 3.4	Correlation function width dependence on total pair momentum. Pion pairs with a large total momentum are more correlated [27]. .	30
811 4.1	no caption	33
812 4.2	no caption	34
813 4.3	no caption	35
814 4.4	no caption	36
815 4.5	no caption	37
821 4.6	no caption [29] [30].	38
822 4.7	no caption [30].	38
823 4.8	no caption [30].	39
824 4.9	no caption [30].	39
825 4.10	no caption [30].	40
826 4.11	no caption [30].	40
827 4.12	no caption [30].	41